Conference Proceedings

The SMS/NanoMed/Sensors 2023 International Joint Conference

Albufeira, Portugal - Oct 25 to 27, 2023

DOI:
https://doi.org/10.26799/cp-sms-nanomed-sensors-2023

Proceedings of the SMS/NanoMed/Sensors 2023 International Joint Conference
Albufeira, Portugal – October 25 – 27, 2023
DOI: https://doi.org/10.26799/cp-sms-nanomed-sensors-2023

Design and Evaluation of an Energy-autonomous Ultra-thin Wireless Sensor Node for Condition Monitoring of Wind Turbine Blades

T. Schaechtle [1,2,*], C. Heim [1], H. Köhler [1], K. Mader [1], A. Binder [3], G. Bruckner [3],
L. M. Reindl [1], S. J. Rupitsch [1]
[1] Laboratory for El. Instrumentation and Emb. Systems, University of Freiburg, Freiburg, Germany
[2] Fraunhofer Institute for Highspeed Dynamics, Ernst Mach-Institute, Freiburg, Germany
[3] Silicon Austrian Labs, Villach, Austria

Abstract

Wind turbines are installed in remote locations and are exposed to harsh environmental conditions, which have a particularly strong impact on their rotor blades. Therefore, it is of great interest to acquire local measurement data to determine the present state of the wind turbine to enable safe and efficient operation.

For this purpose, we present an energy-autonomous, ultra-thin wireless sensor node. The sensor node consists of a planar capacitive sensor for ice layer detection and MEMS accelerometers for modal analysis in regular intervals and continuous peak load detection. The energy-autonomous operation is obtained with a thin-film solar cell designed for low illumination, a constant voltage charging circuitry and a bendable Li-ion rechargeable battery with a height of 450 µm as energy storage. The operational components of the sensor node are evaluated independently, and the wireless sensor node is demonstrated on a small-scale wind turbine blade with a length of 1.07 m.

Keywords: wireless sensor node, energy-autonomous, energy harvesting, flexible electronics, predictive maintenance, wind turbine monitoring, modal analysis, MEMS accelerometers, ice layer detection, capacitive sensor.

1. Introduction

Sensor nodes are a driving element of digitization and are increasingly being deployed in almost every conceivable field such as Smart Home, Smart Agriculture or various industrial applications. With information to be collected in remote or difficult to access locations, wireless communication is often a favoured solution. These wireless sensor nodes can be operated purely passive [1], fully batteryless [2], or with batteries and additional energy harvesting for extended lifetime [3]. Energy harvesting is the capture of ambient energy from the environment, which has been the subject of extensive research in the past decades [4]. With the declining energy consumption of modern sensors and electrical circuitries, it may be of increasing interest for commercial applications.

The utilization of energy-autonomous wireless sensor nodes provides novel monitoring possibilities for wind turbines as a cost-effective and low-maintenance solution for rotating blades. Eigenfrequencies and ice layer thickness are two crucial parameters for monitoring wind turbine blades, which this contribution focuses on [5–7]. The analysis of acceleration can detect temporary mechanical peak loads and identify early stages of permanent damage through methods of structural health monitoring based on a modal analysis [5, 6]. A significant mechanical load on the wind turbine blade is imposed by accumulating an ice layer, which can reach a thickness of several centimeters. This can have a strong influence on the performance or operating times of a wind turbine. Therefore, it is of great interest to detect icing on the wind turbine blades to ensure safe and efficient operation with optimal use of expensive de-icing methods [5, 7].

Ultra-thin and flexible electronics can be integrated onto the curved surfaces of wind turbine blades to minimize aerodynamic impact and extend the operational functionality of wireless sensor nodes [8]. Therefore, in [9], a prototype of a flexible wireless sensor node with solar energy harvesting and a discrete fractional open circuit voltage maximum power point tracking is implemented with a supercapacitor for biometric monitoring. The power management achieves an output of 44.1 µW with a power efficiency of 65 % at 320 lux illumination intensity with a solar cell area of 60 x 72 mm² and an overall thickness of at least 3.5 mm. The discrete DC-DC power management circuitry requires 32.5 µW for operation.
In [10], a multifunctional flexible sensor node for ice layer detection on an aircraft wing is presented. It features a capacitive ice layer detection exploiting the capacitance-to-digital converter (CDC) *AD7142* by *Analog*

DOI: https://doi.org/10.26799/cp-sms-nanomed-sensors-2023

Devices. A compact sensor node is achieved by placing a 2.4 GHz patch antenna and the electrodes for capacitive ice layer detection underneath a solar cell yielding a thickness of approximately 2.6 mm. The prototype consists of a monocrystalline silicon photovoltaic cell with an area of 24 × 19.5 mm² and a power output of 75 mW at standard test conditions AM1.5 at 1 000 W/m², corresponding to direct sunlight at 100 000 lux.

This contribution presents an ultra-thin, flexible and energy-autonomous wireless sensor node, exploiting modern, low-power technologies to integrate ice layer detection, continuous mechanical impact detection and modal analysis to demonstrate the capabilities of energy harvesting.

2. Energy Harvesting Concept

For the energy-autonomous operation of the wireless sensor node, ambient energy is exploited. The fundamental ambient energy sources of thermal, kinetic, light and electromagnetic energy at radio frequencies can be converted for electrical utilization with the well-known principles of energy harvesting [3, 11]. The conversion principles are briefly discussed with regard to their suitability to be employed on a wind turbines rotor blade.

Temperature differences can be converted into electrical energy using thermoelectric generators (TEG) [12, 13]. A temperature difference is potentially occurring between the ambient air and the wind turbine blade due to the high thermal mass. To ensure a good thermal connection to the ambient air, heat sinks with high surface areas are generally exploited [14, 15]. These result in a bulky structure and, together with the low energy conversion efficiencies at small temperature differences, make them inapplicable for this purpose.

Kinetic energy can be converted with piezoelectric, electrostatic, electromagnetic [16–18] or the more recently researched triboelectric nanogenerators (TENG) [19, 20]. There is a variety of application-driven designs for harvesting kinetic energy. Revolving structures, driven by a passing air flow or bending beam structures with flow-induced vibration are exposed to environmental conditions and, therefore, cannot be operated all year round on a wind turbine blade. For this reason, only encapsulated systems are feasible, which however can only extract energy during acceleration, deceleration or elongation of the wind turbine. Since low energy densities are to be expected, along with a limited reduction of the components thickness, their application is only possible at great expense.

Electromagnetic energy at radio frequencies (RF) can be harvested from ambient environment over a vast area due to the widespread deployment of radio technologies [21, 22]. However, the power decreases significantly with greater distance from a source, as described by the Friis equation, yielding in one of the lowest energy densities of the harvesting technologies [3, 4, 23]. This can be illustrated with an exemplary calculation of a typical WIFI technology at 2.4 GHz with 20 dBm transmitted power, dipole antennas for transmitter and receiver with a gain of 2 dBi, where the power is decreased to less than −20 dBm at the receiver after a distance below 2 meters, which corresponds to less than 10 µW. In remote areas, this could only be used as a supplementary solution [10].

This leads to the last energy conversion technology to harvest ambient light with photovoltaic cells. This technology provides one of the highest energy densities and enables ultra-thin and flexible designs [24].

3. Design and Evaluation

The wireless sensor node consists of a flexible polyimide substrate as printed circuit board and rigid commercial off-the-shelf electronics. A partially flexible sensor node is designed by selecting flat, small area rigid electronic components with low-power capabilities. A radio transceiver, several sensors, an energy management with energy harvesting and energy storage are the main components of the wireless sensor node.

An ultra-thin, flexible and energy-autonomous wireless sensor node as shown in Fig. 1 was designed, fabricated and evaluated. In the following, the individual modules are described and evaluated in laboratory setups, and the implemented sensor node is demonstrated on a small-scale wind turbine with the rotor blade’s length of 1.07 m.

DOI: https://doi.org/10.26799/cp-sms-nanomed-sensors-2023

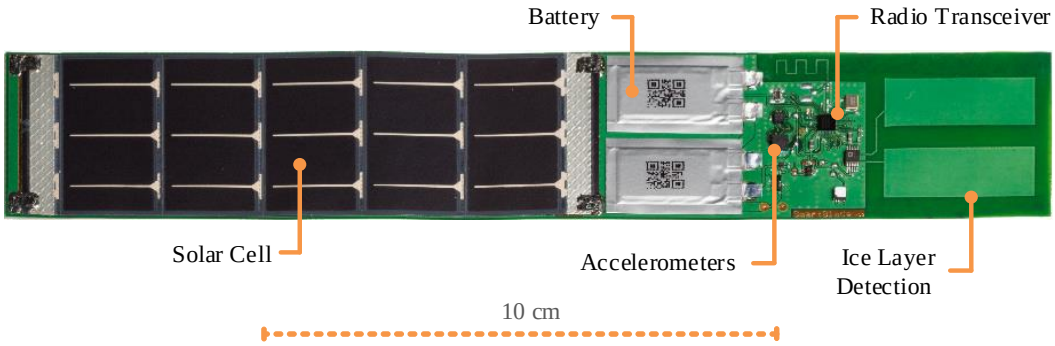

Fig. 1: Photo of the energy-autonomous wireless sensor node on a 200 µm thick polyimide substrate.

3.1. Energy Management

For the energy management, the operating conditions of the solar cell, energy storage and other required voltages of the digital circuitry need to be optimized to ensure minimal losses of the harvested energy to power the sensor node. For this purpose, converter topologies with DC-DC switching regulators are commonly utilized due to their high conversion efficiency [3, 25]. However, the very low, though constant internal consumption of these regulators decreases the efficiency significantly at low currents. Therefore, in this contribution, an energy management designed for low currents is implemented with a linear dropout regulator (LDO) and a careful selection of the components as depicted in Fig. 2. This involves the measurement of the solar cell and the evaluation of the charging circuit's efficiency over a wide range of illumination intensities.

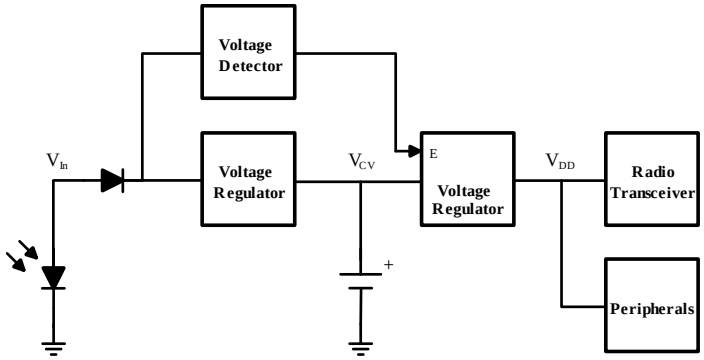

Fig. 2: Schematic of the energy management implemented on the wireless sensor node consisting of a solar cell and two-staged linear voltage regulators to charge the rechargeable battery and supply the electronics. A voltage detector enables the power supply of the subsequent electronics.

First, the energy storage is selected based on geometric and electrical requirements, with emphasis on a compact and flat design. This includes ensuring a peak load current suitable for the wireless transmission of data, a thickness below 1 mm, and a sufficient storage capacity. A detailed evaluation of commercially available technologies indicated that technologies such as ultra-thin supercapacitors or chip-scale solid state batteries with a thickness of less than 1 mm, only allow low discharge currents or low storage capacity. As a result, the novel and promising Li-ion technology *EnerCera*® by *NGK* with a wide temperature range of −40 °C up to 70 °C was selected. The pouch cell *ET271704P-H* with a dimension of 27 x 17 mm² and a thickness of 450 µm provides a capacity of 5 mAh at a nominal voltage of 2.3 V with a favourable discharge voltage profile. It allows for a constant voltage (CV) charging method, which can be implemented cost-effectively and in a compact design with an LDO at a charging voltage of 2.7 V.

For the power management with an LDO, the maximum power point (MPP) of the solar cell is selected to be close to the charging voltage of the battery to maintain low losses. The solar cell is additionally chosen for the poorest light conditions during winter season with low levels of illumination and possible icing on top of it. Therefore, low illumination intensities of 100 lux to 1000 lux are investigated. The *LL200-3-37* solar cell manufactured by *PowerFilms* is specified to have an open circuit voltage of 3.5 V and an MPP of 2.6 V specified at 1000 lux, which closely matches the charging voltage of the battery. The solar cell is evaluated in a dark room chamber by LED lighting adjusted with the light meter *LM631* by *Meterman* to 1000 lux, with the

DOI: https://doi.org/10.26799/cp-sms-nanomed-sensors-2023

resulting power density over the terminal voltage in Fig. 3 a). The solar cell is connected to the electronic load *BK Precision 8600*, without any further components in this measurement. A maximal power density of 0.035 mW/cm² at 2.7 V with a total power of 1.2 mW is obtained.

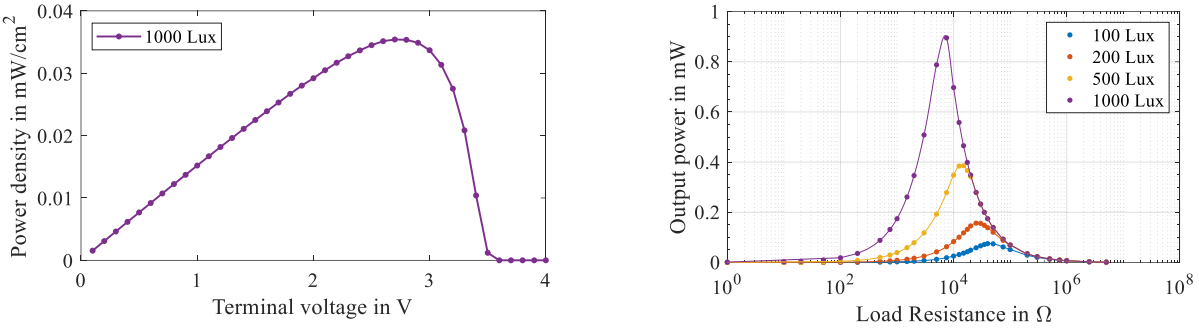

a) b)

Fig. 3: (a) Power density measurement of the solar cell at 1000 lux. (b) Power measurement of the solar cell with blocking diode and first-stage voltage regulator over various load resistance and low illumination intensities.

In Fig. 3 b), an ohmic load is connected after a blocking diode and the first-stage voltage regulator, as depicted in Fig. 2, to obtain the power across the load resistance at low illumination intensities between 100 and 1 000 lux. A blocking diode is necessary to reduce the reverse current from battery to the solar cell at no illumination to a maximum of 0.5 µA. Due to the maximum power point's mismatching and additional electrical losses, a reduced maximal power output of 0.9 mW at 1 000 lux is apparent. Furthermore, the power efficiency of the battery charging circuitry consisting of the blocking diode, the first-stage voltage regulator and the battery in an empty, medium and full state of charge was investigated over an illumination of 100 to 100 000 lux. The power at V_{In} and V_{CV}, as labelled in Fig. 2, was recorded. A power efficiency of the charging circuitry of greater than 88 % for low illumination of 100 to 1000 lux, 86 % at 25 000 lux and 77 to 83 % at 100 000 lux for full and empty battery state was determined.

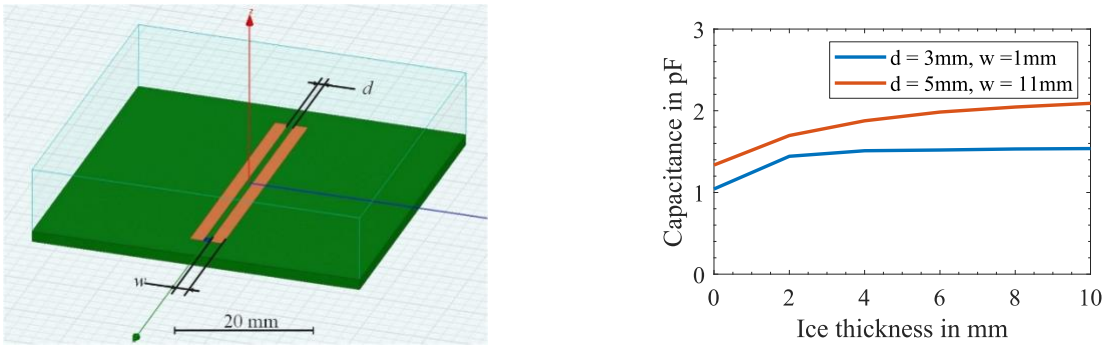

a) b)

Fig. 4: (a) Schematic of two planar electrodes on a FR4 substrate with blue / transparent material with variable thickness on top, featuring approximate electromagnetic properties of ice. (b) Simulation results of the obtained capacitance over the ice thickness for selected electrode geometries.

3.2. Ice Layer Detection

A capacitive fringing field sensor was chosen to locally measure the ice thickness on the leading edge of a wind turbine blade while incorporating a sensor principle with a low geometric profile. The sensor consists of two planar electrode surfaces. Changes of the material in the fringing field result in a change in the capacitance of the sensor. Due to the different permittivities of air, water and ice, the thickness of an ice layer can be estimated [7]. To design the electrodes' width *w* and electrode distance *d* as depicted in Fig. 4 a), a finite element simulation was performed in the high-frequency structure simulator (*HFSS*) by *ANSYS*. As an example, the obtained capacitances of two electrode geometries are shown in Fig. 4 b) from the results of a parameter sweep of *w* and *d* with simulated ice layers from 0 to 10 mm in 1 mm increments. It indicates that larger electrode surfaces lead to a deeper penetration of the fringing fields in the direction of the growing ice layer. To achieve

DOI: https://doi.org/10.26799/cp-sms-nanomed-sensors-2023

sufficient sensitivity for the capacitive sensor in the range of up to 10 mm, an electrode geometry of 11 mm width and 5 mm electrodes distance was chosen.

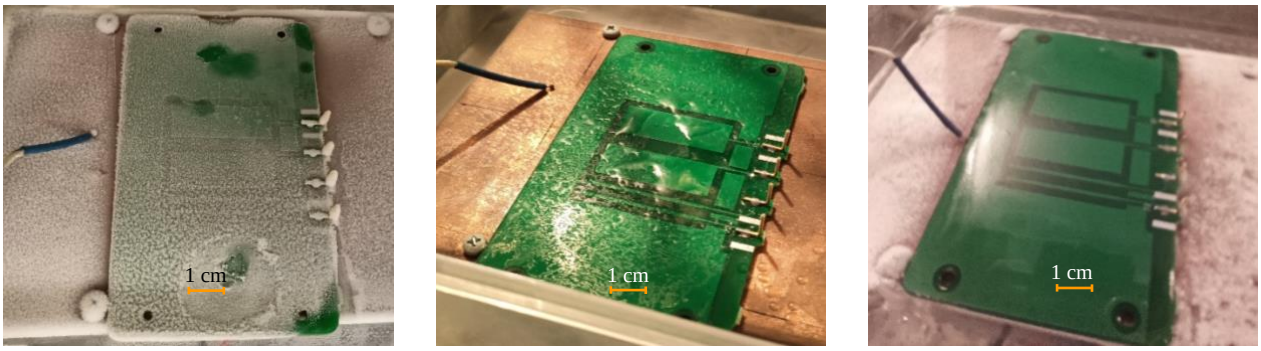

a) b) c)

Fig. 5: Investigation of ice layer deposition (a) Rime ice deposited by ultrasonic atomizer. (b) Spray bottle deposition with droplet formation due to surface tension. (c) Uniformly deposited clear ice layer with combination of ultrasonic atomizer for seed layer and spray bottle deposition.

This geometry was fabricated and evaluated with a reference measurement setup in a climate chamber, allowing for the determination of the ice layer thickness on the capacitive sensor. A tactile measurement of the ice layer thickness is achieved with a three-axis linear stage and a tactile sensor as touch trigger. An ice thickness of approximately 1 mm was incrementally grown. We applied an initial ice seed layer with an ultrasonic atomizer to achieve a uniform coverage during the subsequent manual spray deposition with a pump spray, which was necessary due to the high surface tension of the solder resist as shown in Fig. 5.

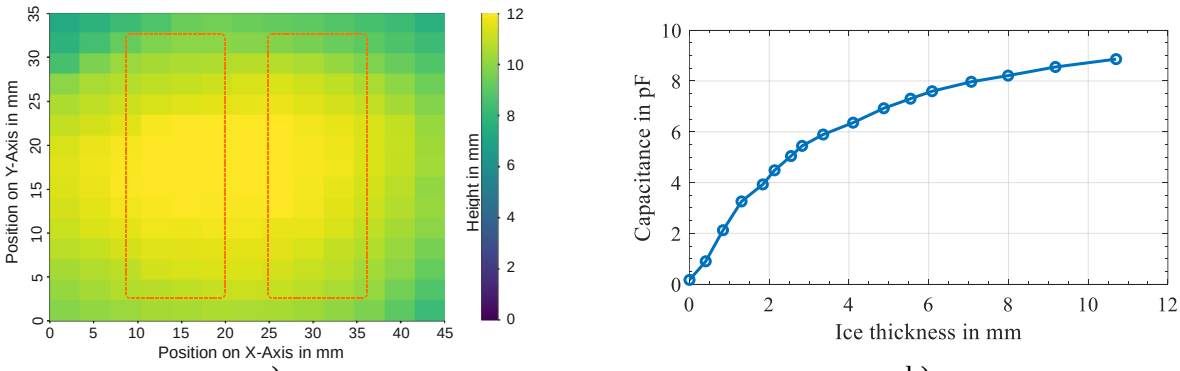

a) b)

Fig. 6: (a) Height profile of the deposited ice layer on the planar capacitive sensor with indicated electrode surfaces obtained with the tactile measurement setup. (b) Extracted capacitance of the electrode surface at stable conditions over the averaged ice layer thickness.

Fig. 6 a) shows a reference measurement of the scanned ice layer thickness at approximately 10 mm, and the averaged spot measurements for all ice heights listed in Tab. 1. The capacitance is measured exploiting the capacitance-to-digital converter *AD7151* by *Analog Devices*. The calibration curve depicted in Fig. 6 b) illustrates the relationship between the observed capacitance and the reference ice thickness derived from the tactile measurement.

Further measurements to evaluate the cross-sensitivity of the capacitive sensor to humidity and temperature were performed in a climate chamber. Only a small change in capacitance of 9.0 ± 1.6 fF was observed at a constant temperature of 30 °C and with a change in relative humidity ranging from 30 to 90 %. To observe the temperature dependency, the absolute humidity was kept approximately constant at 10 ± 2 g/m³ and a capacitance change of 3.0 ± 1.7 fF was obtained with a change in temperature of 10 – 50 °C.

Table 1: Averaged ice height of the ice profile obtained with the tactile measurement setup.

#	1	2	3	4	5	6	7	8	9	10	11	12	13	14	15	16

DOI: https://doi.org/10.26799/cp-sms-nanomed-sensors-2023

Height in mm	0.41 ± 0.11	0.84 ± 0.16	1.31 ± 0.25	1.84 ± 0.28	2.13 ± 0.26	2.55 ± 0.47	2.83 ± 0.53	3.35 ± 0.60	4.10 ± 0.70	4.87 ± 0.76	5.55 ± 0.94	6.09 ± 1.08	7.07 ±1.26	8.00 ± 1.26	9.18 +1.30	10.70 ± 1.10

3.3. Acceleration Analysis

Further analysis of mechanical loads for structural health monitoring can be integrated on an energy-autonomous sensor node with modern MEMS acceleration sensors featuring low-power operation modes. Therefore, a continuous impact detection and modal analysis at regular intervals has been developed. This was previously described in [26] and is presented only briefly in this contribution.
Initially, the edge- and flapwise eigenfrequencies of a statically fixed small-scale wind turbine blade were identified with a scanning laser Doppler vibrometer and a mechanical impulse excitation. The functionality was integrated into the overall system on the flexible circuit board as shown in Fig. 1. The *ADXL372* accelerometer from *Analog Devices* with a measurement range of up to ±200 g is used for continuous impact detection with a threshold value at 30 g. An extended measurement range is required for the higher accelerations occurring during an impact on the small-scale wind turbine blade. For the modal analysis in regular intervals with increased resolution, the *BMA400* accelerometer from *Bosch Sensortec* with its measurement range of up to ±16 g was selected. When an impact occurs, a modal analysis will be performed on the sensor node and the first five eigenfrequencies and amplitudes are determined and transmitted to a base station. Furthermore, the accelerations are recorded at regular intervals for about one second on the wind turbine blade at a sampling rate of 800 Hz and the entire data is transmitted. A frequency spectrum of the occurring accelerations can be computed and stored at the base station. An example of the captured accelerations on a rotating wind turbine blade with an occurring mechanical impact and the corresponding frequency response can be seen in Fig. 7. Changes in the mechanical structure can be detected over a longer period of time from this data by methods of structural health monitoring.

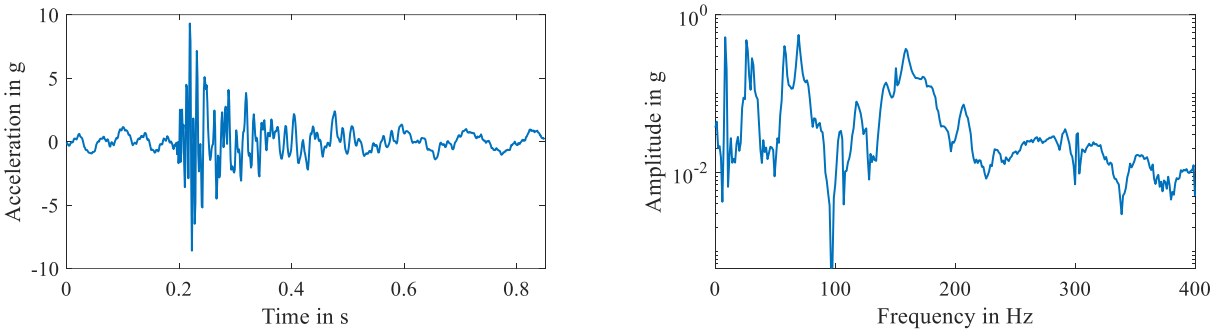

a) b)

Fig. 7: (a) Captured acceleration on the wind turbine blade at 30 rpm with an impact. (b) Frequency spectrum of the captured time domain signal.

4. Demonstration system

The flexible and energy-autonomous wireless sensor node was installed on a small-scale wind turbine blade for demonstration and was operated indoors for several weeks. The wind turbine can be driven by a motor at up to 150 rpm.
A bidirectional proprietary communication was implemented at 2.4 GHz exploiting the low-power transceiver *nRF52840* from *Nordic Semiconductor*. The sensor node records the ice layer thickness, temperature, humidity and battery voltage, which are summarized as sensor data. During a field test, the functionality of the sensor node was tested, with successful detection of randomly applied mechanical impacts both at standstill and during rotation. For the demonstrator, sensor data is collected every 10 seconds and a modal analysis every 50 seconds, then transmitted to the base station, where it is visualized and stored. Fig. 8 shows the demonstration setup and an example of the battery voltage as well as temperature and relative humidity over one week.

DOI: https://doi.org/10.26799/cp-sms-nanomed-sensors-2023

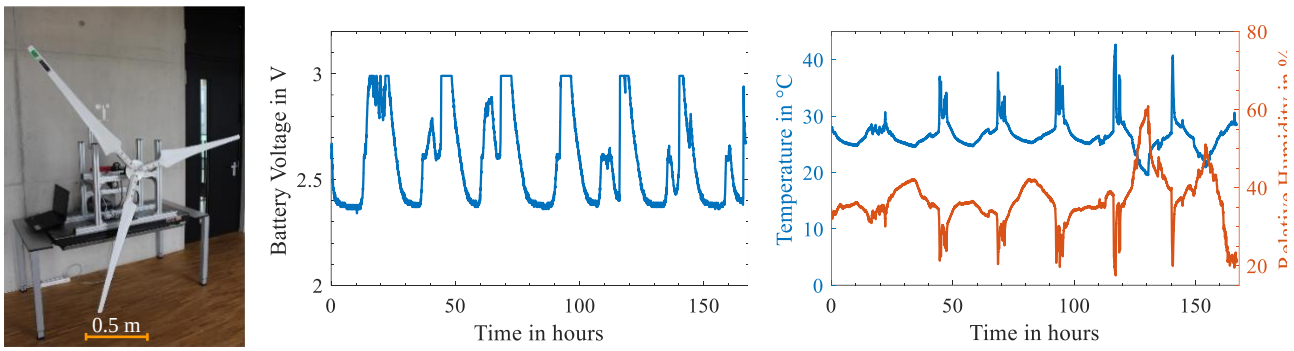

a) b) c)

Fig. 8: (a) Photo of the demonstration setup with a small-scale wind turbine. (b) Battery voltage, (c) temperature and relative humidity over seven days during the field test.

The current consumption and the duration of the tasks for each operation mode are given in Tab. 2 for the current system in Fig. 1 with improved performance.

Table 2: Current consumption of the wireless sensor node at a supply voltage of 1.8 V for different operation modes.

Mode	Current in µA	Duration in ms
Undervoltage shutdown	0.3	-
Deep sleep with RTC	3.37	-
Deep sleet (RTC) + impact detection	4.81	-
Sensor data	4.69	9
Modal analysis	0.36	1 400
Transmit sensor data	7 000	0.997
Transmit modal analysis	11 100	9.7

5. Conclusion

In conclusion, this contribution presents an energy-autonomous wireless sensor node with an area of 38 x 226 mm² and a maximal thickness of 1.2 mm designed for monitoring wind turbine blades. The sensor node integrates a planar capacitive sensor for ice layer detection and MEMS accelerometers for modal analysis with continuous impact detection. The system was demonstrated on a small-scale wind turbine blade, successfully detecting mechanical impacts, ice layer thickness, temperature, humidity, and battery voltage. With the measured current consumption and without energy income, an operation of the sensor node for up to 100 days can be calculated with continuous impact detection, environmental data every 10 min and four modal analyses per day. The flexibility and adaptability of the sensor node provide a promising solution for cost-effective and low-maintenance monitoring of wind turbine blades, addressing crucial parameters such as ice layer thickness and mechanical eigenfrequencies.

Acknowledgements

We gratefully acknowledge the funding of this work by the Austrian Research Promotion Agency (FFG) within the ASSIC project. We sincerely thank NGK for the supply of the rechargeable batteries.

References

1. T. Schaechtle, T. Aftab, L. M. Reindl, and S. J. Rupitsch, “Wireless Passive Sensor Technology through Electrically Conductive Media over an Acoustic Channel,” *Sensors (Basel, Switzerland)*, vol. 23, no. 4, 2023, doi: 10.3390/s23042043.
2. N. Khalid, R. Mirzavand, and A. K. Iyer, “A Survey on Battery-Less RFID-Based Wireless Sensors,” *Micromachines*, vol. 12, no. 7, 2021, doi: 10.3390/mi12070819.
3. M. Prauzek, J. Konecny, M. Borova, K. Janosova, J. Hlavica, and P. Musilek, “Energy Harvesting Sources, Storage Devices and System Topologies for Environmental Wireless Sensor Networks: A Review,” *Sensors*, vol. 18, no. 8, p. 2446, 2018, doi: 10.3390/s18082446.

4. F. Yildiz, "Potential Ambient Energy-Harvesting Sources and Techniques," *Journal of Technology Studies*, vol. 35, no. 1, pp. 40–48, 2009. [Online]. Available: https://eric.ed.gov/?id=ej888131
5. M. McGugan and L. Mishnaevsky, "Damage Mechanism Based Approach to the Structural Health Monitoring of Wind Turbine Blades," *Coatings*, vol. 10, no. 12, p. 1223, 2020, doi: 10.3390/coatings10121223.
6. Z. Gao and X. Liu, "An Overview on Fault Diagnosis, Prognosis and Resilient Control for Wind Turbine Systems," *Processes*, vol. 9, no. 2, p. 300, 2021, doi: 10.3390/pr9020300.
7. K. Wei, Y. Yang, H. Zuo, and D. Zhong, "A review on ice detection technology and ice elimination technology for wind turbine," *Wind Energy*, vol. 23, no. 3, pp. 433–457, 2020, doi: 10.1002/we.2427.
8. D. Corzo, G. Tostado-Blázquez, and D. Baran, "Flexible Electronics: Status, Challenges and Opportunities," *Front.Electron.*, vol. 1, 2020, doi: 10.3389/felec.2020.594003.
9. W. Y. Toh, Y. K. Tan, W. S. Koh, and L. Siek, "Autonomous Wearable Sensor Nodes With Flexible Energy Harvesting," *IEEE Sensors J.*, vol. 14, no. 7, pp. 2299–2306, 2014, doi: 10.1109/JSEN.2014.2309900.
10. W. Stocksreiter and H. Zangl, "Compact Multifunctional Wireless Capacitive Sensor System and Its Application in Icing Detection," *Sensors (Basel, Switzerland)*, vol. 19, no. 24, 2019, doi: 10.3390/s19245562.
11. R. V. Prasad, S. Devasenapathy, V. S. Rao, and J. Vazifehdan, "Reincarnation in the Ambiance: Devices and Networks with Energy Harvesting," *IEEE Commun. Surv. Tutorials*, vol. 16, no. 1, pp. 195–213, 2014, doi: 10.1109/SURV.2013.062613.00235.
12. *Miniature Thermoelectric Generators - thermoelectric solutions for small-scale green energy harvesting.* [Online]. Available: https://www.tec-microsystems.com/products/thermoelectric-generators/index.html (accessed: Sep. 4 2020).
13. D. Champier, "Thermoelectric generators: A review of applications," *Energy Conversion and Management*, vol. 140, pp. 167–181, 2017, doi: 10.1016/j.enconman.2017.02.070.
14. M. Freunek, M. Müller, T. Ungan, W. Walker, and L. M. Reindl, "New Physical Model for Thermoelectric Generators," (in En; en), *J. Electron. Mater.*, vol. 38, no. 7, pp. 1214–1220, 2009, doi: 10.1007/s11664-009-0665-y.
15. M. Müller, M. Freunek, T. Ungan, and L. M. Reindl, "Wandler für energieautarke Mikrosysteme. Stand der Technik kommerzieller Energiewandler," *tm - Technisches Messen*, vol. 76, no. 12, p. 738, 2009, doi: 10.1524/teme.2009.0979.
16. R. Caliò *et al.*, "Piezoelectric Energy Harvesting Solutions," *Sensors*, vol. 14, no. 3, pp. 4755–4790, 2014, doi: 10.3390/s140304755.
17. H. Fu *et al.*, "Rotational energy harvesting for self-powered sensing," *Joule*, vol. 5, no. 5, pp. 1074–1118, 2021, doi: 10.1016/j.joule.2021.03.006.
18. I. Neri, F. Travasso, R. Mincigrucci, H. Vocca, F. Orfei, and L. Gammaitoni, "A real vibration database for kinetic energy harvesting application," *Journal of Intelligent Material Systems and Structures*, vol. 23, no. 18, pp. 2095–2101, 2012, doi: 10.1177/1045389X12444488.
19. F.-R. Fan, Z.-Q. Tian, and Z. Lin Wang, "Flexible triboelectric generator," *Nano Energy*, vol. 1, no. 2, pp. 328–334, 2012, doi: 10.1016/j.nanoen.2012.01.004.
20. J. Yan, Z. Tang, N. Mei, D. Zhang, Y. Zhong, and Y. Sheng, "Research Progress on the Application of Triboelectric Nanogenerators for Wind Energy Collection," *Micromachines*, vol. 14, no. 8, 2023, doi: 10.3390/mi14081592.
21. "Harvesting Wireless Power: Survey of Energy-Harvester Conversion Efficiency in Far-Field, Wireless Power Transfer Systems," *IEEE Microwave*, vol. 15, no. 4, pp. 108–120, 2014, doi: 10.1109/MMM.2014.2309499.
22. J. Garnica, R. A. Chinga, and J. Lin, "Wireless Power Transmission: From Far Field to Near Field," *Proc. IEEE*, vol. 101, no. 6, pp. 1321–1331, 2013, doi: 10.1109/JPROC.2013.2251411.
23. M. Cansiz, D. Altinel, and G. K. Kurt, "Efficiency in RF energy harvesting systems: A comprehensive review," *Energy*, vol. 174, pp. 292–309, 2019, doi: 10.1016/j.energy.2019.02.100.
24. H. Sharma, A. Haque, and Z. A. Jaffery, "Solar energy harvesting wireless sensor network nodes: A survey," *J. Renewable Sustainable Energy*, vol. 10, no. 2, 2018, doi: 10.1063/1.5006619.
25. Q. Lian, P. Han, and N. Mei, "A Review of Converter Circuits for Ambient Micro Energy Harvesting," *Micromachines*, vol. 13, no. 12, 2022, doi: 10.3390/mi13122222.
26. T. Schaechtle, C. Heim, G. Bruckner, A. Binder, L. Reindl, and S. Rupitsch, "Energy-Autonomous Wireless Sensor Node for Monitoring of Wind Turbine Blades," in *Lectures*, Nürnberg, May. 2023 - May. 2023, pp. 106–107.

Proceedings of the SMS/NanoMed/Sensors 2023 International Joint Conference
Albufeira, Portugal – October 25 – 27, 2023
DOI: https://doi.org/10.26799/cp-sms-nanomed-sensors-2023

Interaction of Microparticles of Different Rigidities with Serum and Plasma Proteins

E. Gerasimovich[1,2], G. Nifontova[3], I. Nabiev [1-3], A. Sukhanova[3]
[1]Life Improvement by Future Technologies (LIFT) Center, Skolkovo, 143025 Moscow, Russia
[2]Laboratory of Nano-Bioengineering, National Research Nuclear University MEPhI (Moscow Engineering Physics Institute), 115409 Moscow, Russia
[3]Laboratoire de Recherche en Nanosciences, LRN-EA4682, Université de Reims Champagne-Ardenne, 51100 Reims, France

Abstract

Polyelectrolyte microparticles (MPs) and microcapsules obtained using layer-by-layer deposition can be used in various applications in the field of biomedicine. However, their interaction with components of biological media is known to affect their properties and alter their activity. Understanding the factors influencing this interaction is essential for rational design of particle-based applications. In this study, we compared the interactions of polyelectrolyte MPs of different structures with serum and plasma proteins. We used the layer-by-layer approach to obtain polyelectrolyte MPs with core/shell and shell structures. Then, the MPs were incubated with human serum or plasma at 37°C for 24 h. Absorbed proteins were eluted and analyzed by polyacrylamide gel electrophoresis under denaturing conditions. The protein composition was analyzed by means of MALDI-TOF mass spectrometry. Most proteins identified in the samples were associated with the immune system and blood coagulation cascade. It was demonstrated that the presence of several proteins in the adsorption layer on the MPs varied depending on the MP structure. In addition, the type of blood derivative used for incubation with the MPs also affected the protein composition of the adsorption layer.

Keywords: polyelectrolyte microparticles, drug delivery systems, layer-by-layer approach, protein adsorption

1. Introduction

Engineering of novel drug delivery systems specifically interacting with diseased cells is of great interest for biomedicine [1]. Polyelectrolyte microparticles (MPs) and microcapsules with a shell made of biocompatible polymers can serve as microcontainers with adjustable characteristics, including the size, structure, and surface properties [2]. Modification of the MP structure allows controlling the release of their inner content by physical (ultrasound or magnetic field) or chemical (pH or ionic strength) stimuli and ensuring specific interaction with the target via conjugated recognizing molecules [3].

Physicochemical and biochemical properties of polyelectrolyte MPs undergo modification in biological media. The surface of microcapsules absorb biomolecules from blood, which leads to the formation of the so-called protein corona [4]. This modification may alter the targeting capacity of MPs. Polymer-coated silica particles carrying affibodies on the surface exhibited a significantly weakened specific association with cancer cells after incubation with human serum; however, the modification of the particle surface with HSA considerably enhanced particle–cell association [5]. Another study demonstrated that the targeting capacity of polymeric capsules and core/shell particles functionalized with monoclonal antibodies (mAbs) could be preserved in the presence of the protein corona; however, the composition of the protein corona differed between the capsules and particles [6]. Recently, modification of polymeric microcapsules with different proteins, including human immunoglobulin (IgG), which is abundant in serum, was demonstrated to reduce their cytotoxicity [7].

Study of protein adsorption is an important issue in designing drug delivery systems based on polymeric microcapsules because it can affect both effectiveness and safety of these systems. However, previous studies on this issue are few and lack systematic assessment of the influence of the MP properties on the composition of adsorbed proteins. In this study, we obtained model polyelectrolyte MPs with different structures and analysed the differences between them in protein adsorption by means of SDS-PAGE and MALDI-TOF mass spectrometry.

2. Materials and Methods

2.1. Synthesis of Calcium Carbonate Cores

DOI: https://doi.org/10.26799/cp-sms-nanomed-sensors-2023

Calcium carbonate cores were synthesized from 0.33 M Na_2CO_3 and 0.33 M $CaCl_2$ solutions in 44% aqueous solution of glycerol as described before [8]. The size and shape of the obtained $CaCO_3$ MPs were assessed by means of optical microscopy using an Axio Observer 3 microscope (Zeiss, Jena, Germany).

2.2. Preparation of Polyelectrolyte Microparticles with Different Structures

Calcium carbonate cores were used as templates for the fabrication of polyelectrolyte MPs by means of layer-by-layer deposition as described before [9]. Poly(allylamine hydrochloride) (PAH, Mw≈65,000 Da, Merck Group, Sigma-Aldrich), poly(sodium 4-styrenesulfonate) (PSS, Mw≈70,000 Da, Merck Group, Sigma-Aldrich), and poly(acrylic acid sodium salt) (PAA, Mw≈15,000 Da, Merck Group, Sigma-Aldrich) were applied onto MPs to form a multilayer shell of the following structure: PAH/PSS/PAH/PSS/PAH/PSS/PAH/PSS/PAH/PAA. To obtain shell structures, MPs were incubated in the presence of 0.5 M EDTA (pH 8.0) under constant stirring overnight. After the incubation, the resulting shell microcapsules were collected by centrifugation and washed with ultrapure water three times. At the final step, the microcapsules were resuspended in 50 mM sodium phosphate buffer, pH 8.0.

2.3. Incubation of Microparticles with Serum and Plasma and Their SDS-PAGE Analysis

Equivalent amounts of MPs ($4*10^7$ particles) dispersed in 50 μL of 50 mM sodium phosphate buffer (pH 8.0) were incubated with 250 μL of human serum (HS), human plasma (HP) or PBS (control samples) under constant shaking at 300 rpm in an Eppendorf ThermoMixerC (Eppendorf, Germany) at 37°C for 24 h. After the incubation, the microcapsules were separated by centrifugation for 20 min at 16,873 *g* and washed with 0.5 mL of PBS five times by means of centrifugation (2 min, 16,873 *g*) and resuspension. Then, 50 μL of Sample Buffer (Sigma Aldrich) was added to the pellets, and they were incubated for 20 min at 95°C to elute proteins from the surface of the microcapsules. After the incubation, the microcapsules were separated by centrifugation for 5 min at 16,873 *g*, and the supernatants were transferred to fresh test tubes. The samples were analysed by means of SDS-PAGE in a 5% concentrating gel and a 7% resolving gel. Each gel contained one lane of prestained protein molecular weight markers (Spectra™ Multicolor High Range Protein Ladder, Thermo Fisher Scientific, USA). The images of the gels were captured using a ChemiDoc XRS+ imaging system (Bio-Rad Laboratories Ltd., Hertfordshire, UK). The apparent molecular weights of protein bands were calculated from calibration curves based on the molecular weight of the protein markers on each gel.

2.4. Mass-spectrometry Sample Preparation and Analysis

The bands intended for MALDI-TOF mass-spectrometry analysis were cut from the gels and stored at 4°C. Sample preparation for the analysis was carried out in the Human Proteome Core Facility of the Institute of Biomedical Chemistry, Moscow, Russia. Mass spectra were obtained using an Ultraflex II BRUKER MALDI time-of-flight mass spectrometer (Germany) equipped with an UV laser (Nd) in the positive ion mode using a reflectron; the accuracy of the measured masses was 70 ppm. Fragmentation spectra were obtained in the TOF/TOF (LIFT) mode. Protein identification was performed using the Mascot software (www.matrixscience.com). The search was carried out in the Swissprot database among the proteins of all organisms with the above accuracy, with the possible oxidation of methionine by atmospheric oxygen and the possible modification of cysteine by acrylamide taken into account.

3. Results and Discussion

At the first stage of our study, $CaCO_3$ cores with an average size of 2.6 μm were obtained in a 44% glycerol aqueous solution. These cores were used as templates to engineer core/shell and shell MPs with the layer structure of $(PAH/PSS)_4$/PAH/PAA and a strong negative surface charge.

DOI: https://doi.org/10.26799/cp-sms-nanomed-sensors-2023

Figure 1A shows the SDS-PAGE gel with samples containing proteins eluted from the surface of MPs after their incubation with serum or plasma. The relative intensities of the bands indicated in the gel are shown in Fig. 1B. We used MALDI-TOF mass-spectrometry to identify proteins in five protein bands detected in the samples. Band 4 with an apparent molecular weight of 67 kDa, which contained human serum albumin, was identified in all samples. However, the relative intensity of this band was higher in control samples (neat serum and plasma) than in the samples from the MP surface. The other identified bands were detected only in experimental samples, which indicates enrichment of the MP surface with these proteins compared with neat serum and plasma. In bands 1 and 2 with apparent molecular weights of 90 and 82 kDa, respectively, proteins involved in blood coagulation were identified. Interestingly, band 1 was found only in eluates from MPs incubated with serum, while band 2, only in eluates from MPs incubated with plasma. The relative intensities of both bands were higher in samples obtained from shell MPs. The proteins identified in bands 3 and 5 with apparent molecular weights of 72 and 42 kDa, respectively, were related to the immune system. The relative intensities of band 3 were comparable in all samples. At the same time, the relative intensities of band 5 were higher in samples obtained from core/shell MPs. Thus, we identified several differences in the composition and relative intensities of protein bands in eluates from MPs with different structures, as well as MPs incubated with different blood derivatives (serum or plasma). These differences may affect further biological interactions of MPs after their contact with blood components.

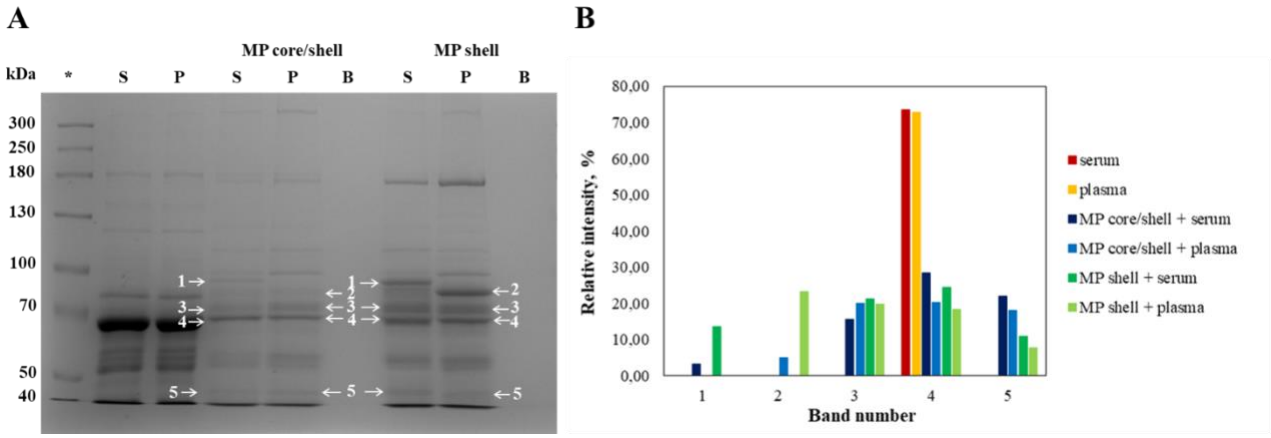

Fig. 1: (A) SDS-PAGE gel of human serum/plasma proteins obtained from the surface of core/shell and shell MPs after incubation at 37°C for 24 h. The arrows indicate the bands of interest; the bands of protein markers with specified molecular weights (kDa, *) are present in each lane. (B) The relative intensities of protein bands in the gel.

4. Conclusion

Understanding the factors affecting the interaction of polyelectrolyte MPs with components of biological media is crucial for their application in the field of biomedicine. We have obtained model polyelectrolyte MPs with different structures (core/shell and shell). Experiments have shown differences in the composition and relative amounts of proteins absorbed on MPs differing in structure. In addition, the type of blood derivative (serum or plasma) also affects the spectrum of protein adsorbed on the MPs. These results can be used for improving the design of MP-based biomedical applications.

Acknowledgements

The work related to investigation of interaction of microparticles with serum and plasma proteins was supported by the Russian Science Foundation (RSF), grant no. 22-75-10103; the work related to the synthesis of materials used in the study was supported by the RSF, grant no. 21-79-30048.

References

1. A. Mateos-Maroto, L. Fernandez-Pena, I. Abelenda-Nunez, F. Ortega, G. R. Rubio, and E. Guzman, “Polyelectrolyte Multilayered Capsules as Biomedical Tools,” *Polymers (Basel)*, vol. 14, p. 479, 2022.
2. X. Zan, A. Garapaty, and J. A. Champion, “Engineering Polyelectrolyte Capsules with Independently Controlled Size and Shape,” *Langmuir*, vol. 31, pp. 7601-7608 , 2015.

DOI: https://doi.org/10.26799/cp-sms-nanomed-sensors-2023

3. J. Li, B. V. Parakhonskiy, and A. G. Skirtach, "A decade of developing applications exploiting the properties of polyelectrolyte multilayer capsules," *Chem. Commun.*, vol. 59, no. 7, pp. 807–835, 2022.
4. M. P. Monopoli, C. Åberg, A. Salvati, and K. A. Dawson, "Biomolecular coronas provide the biological identity of nanosized materials," *Nat. Nanotechnol.*, vol. 7, no. 12, pp. 779–786, 2012.
5. Q. Dai et al., "Targeting Ability of Affibody-Functionalized Particles Is Enhanced by Albumin but Inhibited by Serum Coronas," *ACS Macro Lett.*, vol. 4, no. 11, pp. 1259–1263, 2015.
6. Q. Dai et al., "Monoclonal antibody-functionalized multilayered particles: Targeting cancer cells in the presence of protein coronas," *ACS Nano*, vol. 9, no. 3, pp. 2876–2885, 2015.
7. F. A. de Oliveira, L. J. C. Albuquerque, C. E. Castro, K. A. Riske, I. C. Bellettini, and F. C. Giacomelli, "Reduced cytotoxicity of nanomaterials driven by nano-bio interactions: Case study of single protein coronas enveloping polymersomes," *Colloids Surfaces B Biointerfaces*, vol. 213, p. 112387, 2022.
8. D. Kalenichenko, G. Nifontova, A. Karaulov, A. Sukhanova, and I. Nabiev, "Designing functionalized polyelectrolyte microcapsules for cancer treatment," *Nanomaterials*, vol. 11, p. 3055, 2021.
9. G. Nifontova et al., "Next-Generation Theranostic Agents Based on Polyelectrolyte Microcapsules Encoded with Semiconductor Nanocrystals: Development and Functional Characterization," *Nanoscale Res. Lett.*, vol. 13, no. 30, pp. 1-12, 2018.

Proceedings of the SMS/NanoMed/Sensors 2023 International Joint Conference
Albufeira, Portugal – October 25 – 27, 2023
DOI: https://doi.org/10.26799/cp-sms-nanomed-sensors-2023

Flexible copper nanowire-based electrodes: Structure, morphology, Optical and mechanical properties for soft electronics

Nicholas W. Hoy, Lekhetho S. Mpeta and Pontsho S. Mbule*
Department of Physics, CSET, University of South Africa, Johannesburg, 1710, South Africa
*mbuleps1@unisa.ac.za

Abstract

Copper nanowires (CuNWs) were synthesized using hydrothermal method and deposited onto flexible polymer substrates to make films acting as electrodes for possible application as soft electronics. Substrates used were polyethylene terephthalate (PET), polyethylene naphthalate (PEN), Polycarbonate (PC) and Polyethersulfone (PES). Aluminium-doped ZnO nanoflakes (i.e., AZO-NFs) was coated onto CuNWs to act as a protective layer against oxidation. The structure and morphology of the samples were studied by XRD, AFM and HRSEM, respectively. UV-Vis technique was used to determine the light transmittance through the prepared electrodes. The mechanical (stress-strain) properties of the prepared electrodes were also studied. The yield strength, ultimate strength, Young's modulus and resilience are amongst the parameters that were evaluated and are discussed in detail. This work illustrates that PET and PEN offers the potential to be used as transparent flexible substrate in polymer solar cells, as both substrates possess excellent transmittance even when they have been coated with a thin layer of CuNWs and AZO nanoflakes.

Keywords: Copper nanowires; hydrothermal; mechanical properties; flexibility; electrode; polymer substrate; aluminium-doped zinc oxide; gallium-doped zinc oxide.

1. Introduction

Transparent flexible electrodes offer a unique and promising avenue for research owing to the large number of applications in devices such as solar cells [1], touch screens [2], infrared detectors [3], and organic light emitting diodes [4]. Additionally, the flexibility of the electrode will allow it to be moulded and shaped into whatever shape or size its specific application will require allowing for more widespread usage of such a device in different fields and applications.

In the application of flexible solar cells, the requirement of the electrode being transparent has the trade-off and the usage of a wide bandgap. While a wide bandgap material cannot absorb energy using lower-energy photons, a smaller bandgap can. However, energy absorbed from high-energy photons from the smaller bandgaps results in these photogenerated charges to lose most of the energy which is caused by the thermalization that takes place for the electrons to travel out of a material. Regardless of which bandgap is used a large portion of any potential solar energy is lost [5]. Additionally, energy loss due to series resistance can be reduced due to the higher voltage that can be reached with wide bandgap materials [6]. The usage of wide bandgaps also encourages the use and study of multijunction cells which would have the potential to be far more efficient than other commercially used solar cells. Thin metal foils have been found to be especially flexible due to the high ductility of metals allowing for the usage of these foils in flexible electrodes [7]. Of these, stainless-steel foil is the most commonly used metal substrate due to its excellent thermal and chemical stability as well as its low cost and has been used in flexible solar cells since the 1980's [8]. Metal foils initially seem like a promising candidate also due to their good electrical conductivity which results in a lower resistance as well as fast ion and electron transmission [9]. Due to the excellent thermal stability that the metal substrates have, it allows them to be able to undergo higher processing temperatures allowing for various different deposition methods for later stages of the electrode synthesis process. Additionally, metal nanowires are more flexible than other brittle inorganic metal oxides. Of the viable metals that can be used as metal nanowires (including gold and silver) copper is the most practical to be used as it is much cheaper than silver and gold while still having an excellent resistivity (1.67×10^{-8} Ωm) [10]. For the usage of transparent flexible electrodes in solar cells, it is important that both the substrate and the electrode layer are transparent, flexible and, can withstand certain amounts of stresses that might be applied to it in its everyday use on a device. As the substrate and bottom electrode material are on top of each other in solar cells and impact each other, studying both simultaneously will have more meaningful and impactful results in the long term. Thus, in this work both will be examined in order to produce a transparent flexible organic based solar cell.

DOI: https://doi.org/10.26799/cp-sms-nanomed-sensors-2023

2. Experimental section

2.1. Materials

The following materials were used for CuNWs synthesis without any further purification and were obtained from Sigma-Aldrich: copper (II) chloride ($CuCl_2$) (99.999% trace metal basis), L-Ascorbic acid ($C_6H_8O_6$) (ACS reagent ≥ 99%), octadecylamine (ODA)($C_{18}H_{39}N$) (≥ 99.0% GC), n-hexane (≥ 98% GC) and, isopropanol (anhydrous 99.5%), potassium chloride (KCl), iron ferricyanide, iron ferrocyanide, potassium chloride. The following materials were used for AZO-NFs: zinc acetate ($Zn(CH_3CO_2)_2$) (99.99% trace metals basis), sodium hydroxide (NaOH) (≥98% reagent grade pellets) and aluminium nitrate nonahydrate ($Al(NO_3)_3{\cdot}9H_2O$) (ACS reagent ≥ 98%). The polymers substrates used were purchased from Sigma – Aldrich and they are polyethylene terephthalate (PET), polyethylene naphthalate (PEN), Polycarbonate (PC) and Polyethersulfone (PES).

2.2. CuNWs synthesis

Ultra-long and thin CuNWs were synthesized using slightly modified hydrothermal method found in Wang et al [11] but using the same ratios. Initially 0.0607 g copper chloride (5.65 mmol/L) and 0.0394 g ascorbic acid (2.8 mmol/L) were stirred together with 40 mL of deionized water completely dissolving the solution. Then 0.5713 g of ODA (26.5 mmol/L) was also stirred separately in 40 mL of deionized water until it was also dissolved completely. The mixtures were then poured into a larger beaker which was then magnetically stirred for one hour until the final mixture was a blue emulsion which was then placed into an autoclave and then in an oven heated at 120 ℃ for 20 hours.

During the synthesis procedure unwanted by-products such as copper nanoparticles (CuNPs) also formed and needed to be removed. The final CuNWs solution was first mixed with 80 mL of deionized water and centrifuged at 2500 rpm for five minutes to remove any excess reactants in the solution. Thereafter, the solution was mixed with an equal amount of n-hexane and deionized water to separate the CuNWs from the CuNPs. This has been reported before by Kang et al [12]. This step was repeated five more times before the final product was dispersed in isopropanol.

2.3. AZO-NFs synthesis

2 g of zinc acetate was added into 10.9 mL of deionized water and stirred until it was completely dissolved. While the initial solution mixed, 0.436 g of NaOH was mixed with 10.9 mL of deionized water and stirred until it was completely dissolved as well. This solution was then added drop wise into the zinc acetate solution. Thereafter, 0.08345 g (2 mol%) of $Al(NO_3)_3.\ 9H_2O$ was stirred with 5 mL of deionized water and then added to the zinc acetate solution drop wise. The solution was then left to stir for four hours @ 850 rpm. During the entire process the solutions were kept at 65 ^oC on a hot plate to encourage the growth of the nanoflakes. The final NFs were washed via centrifugation at 5000 rpm for two minutes which resulted in the AZO-NFs to gather at the bottom of the holder and the water along with unwanted chemicals were removed via a pipette, thereafter ethanol was added, and the centrifugation process was repeated three more times to ensure the AZO-NFs were cleaned.

2.4. Deposition of CuNWs onto polymer substrates

The polymer substrates were ultrasonically washed with deionized water, ethanol and then were blown by air to dry. CuNWs were then deposited onto the polymer substrates via drop casting method, which yielded an equal distribution of the nanowires. For the CuNWs coating with AZO-NFs, the spin-coating technique was used and the solutions were spin-coated over the copper nanowires at 2000 rpm.

2.5. Characterization techniques

The surface morphology and elemental composition of the deposited films were analyzed using a JEOL JSM-7800F field emission scanning electron microscopy (FESEM) which is coupled with an Oxford Aztec 350 X-Max80 electron dispersive spectroscopy (EDS). To determine the phase and crystal structure of the prepared CuNWs, Rigaku smartLab X-ray diffractometer (Cu Kα, 45 kV and 200 mA) was used. The optical transmittance of the films on polymer substrates was also obtained using a Perkin Elmer Lambda 650 S UV/VIS Spectrophotometer. The roughness of the films was obtained using a WITec alpha300 A AFM microscope. The mechanical (stress – strain) properties of the prepared electrodes were determined using a Deben Tensile 200N microtester.

DOI: https://doi.org/10.26799/cp-sms-nanomed-sensors-2023

3. Results and discussion

3.1 XRD analysis

The XRD patterns in Figure 1 shows that CuNWs have the characteristic peaks at ~2θ = 43.36° and 50.64° corresponding to the (111) and (200) lattice planes, respectively. The XRD patterns corresponds to the standard JCPDS with card no: 03-065-9026. No additional impurities were observed. This distribution of copper face- cantered cubic structures has a preferred orientation of (111) indicating the high purity of the CuNWs. The XRD patterns for AZO-NFs showed an amorphous nature, with preferred orientation of (200). The intense and broad diffraction peak between 2θ = 15° and 25° was detected and can be attributed to the polymer substrates used.

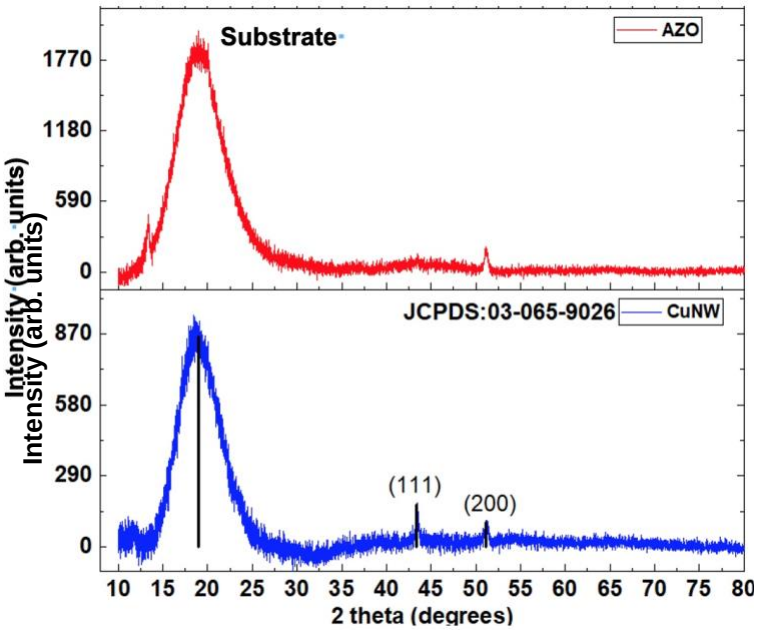

Figure 1: XRD pattern of the CuNWs, AZO-NFs and GZO-NFs on a PES polymer substrate.

3.2 SEM and EDS analysis

Figure 2 (a-c) present the SEM images of CuNWs, and AZO-NFs deposited on a polymer substrate, while Figure 2 (c-d) shows their EDS spectra. As can be observed, ultra-long and smooth CuNWs were successfully synthesized and cleaned to remove unwanted by-products that would impact the properties of the film such as the transmittance and electrical conductivity. The average diameter of the CuNWs was estimated from the images to be ~117.75 nm with an ultra-long length of ~50 μm. This will result in a larger aspect ratio which has been found in other studies to result in the lowering of the sheet resistance of the electrode due to the increased connectivity between the various wires across the substrate [13]. The smoothness of the wires is also important to note as smoother nanowires have been reported to reduce light scattering effects of the film which directly impact the transmittance of the film and thus crucial to know [14]. The nanoflakes can clearly be seen to be well distributed across the polymer film as well as being layered on top of one another which would be beneficial for the protection of the CuNWs against potential oxidation. The EDS spectra confirmed the elemental composition of the prepared materials. Figure 3 shows the elemental mapping which indicate a good and uniform surface distribution.

DOI: https://doi.org/10.26799/cp-sms-nanomed-sensors-2023

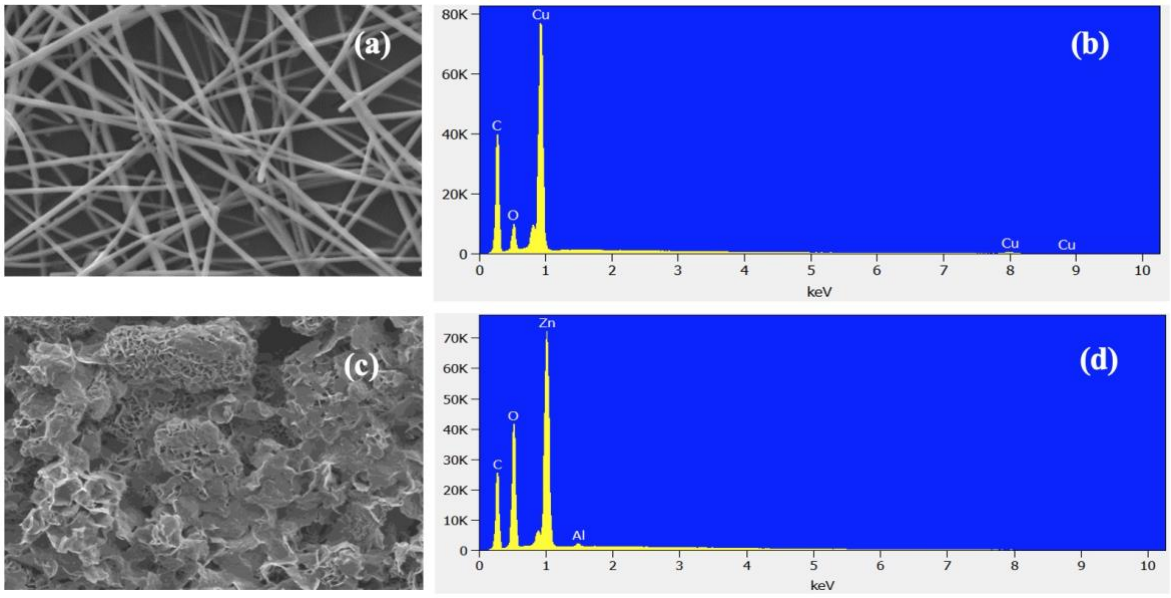

Figure 2 (a-d): SEM images and EDS of CuNWs and AZO-NFs.

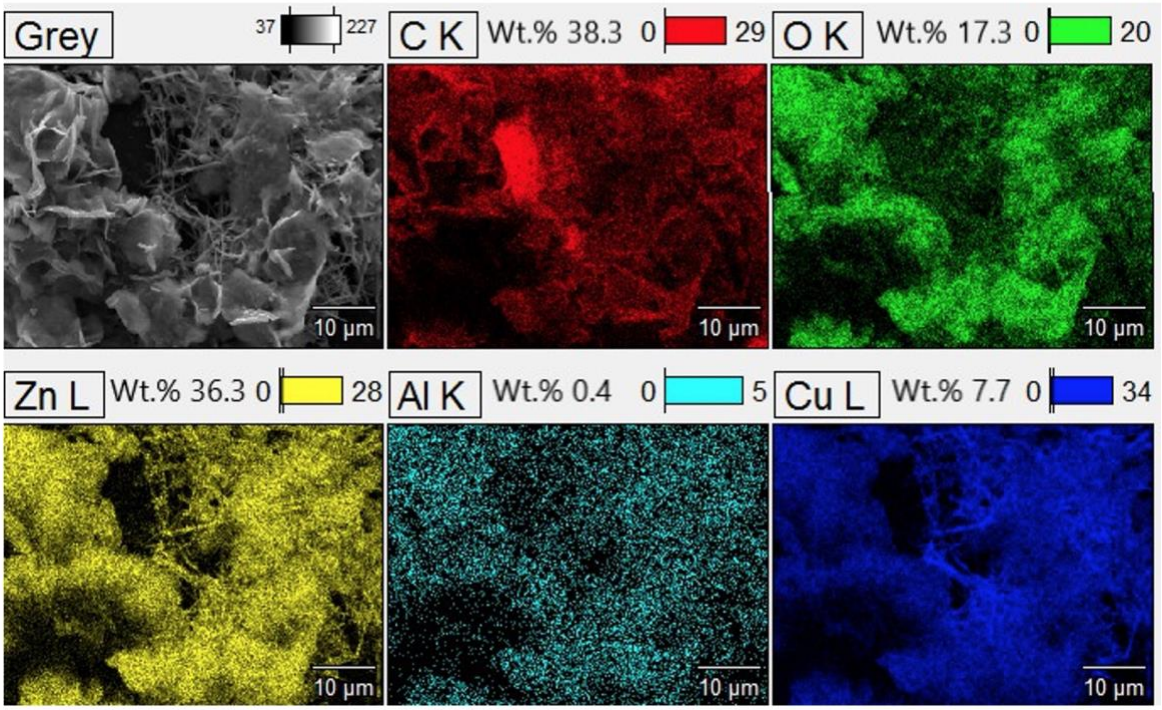

Figure 3: Elemental mapping of CuNWs coated with AZO-NFs

3.3 AFM analysis

The AFM analysis was done to observe the roughness of the deposited films which are recorded in Table 1. As shown in Figure 4, the roughness of the films was observed to increase with the addition of the coating layers which was anticipated. The roughness of the films can contribute to an increase of light trapping in solar cell devices application which may result in the reflection losses being reduced. The CuNWs deposited on PEN substrate showed lower roughness of ~46.35, as compared to other substrates.

DOI: https://doi.org/10.26799/cp-sms-nanomed-sensors-2023

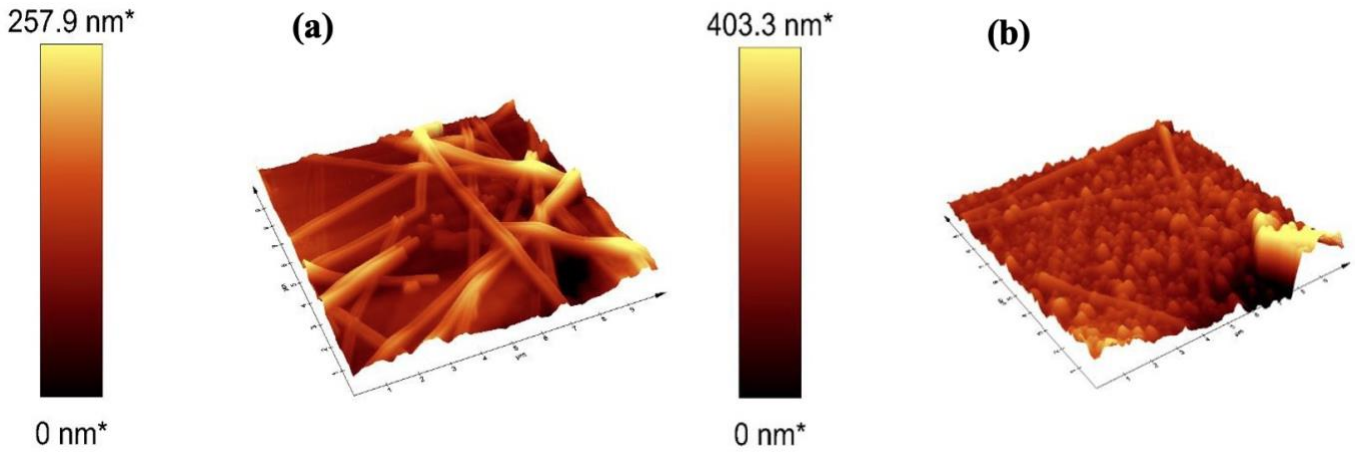

Figure 4: AFM images of (a) CuNWs and (b) CuNWs coated with AZO-NFs

Table 1: Roughness values (nm) of the various substrates and AZO-NFs layer deposited onto them

	PC	PET	PES	PEN
		Layer roughness (nm)		
CuNWs	109.01	73.24	77.51	46.35
CuNWs/AZO-NFs	154.28	318.09	455.59	347.00

3.4 Optical transmittance analysis

The optical transmittance of the prepared films was studied. PET showed a relatively higher transmittance of an average of 88.64% across the entire visible range, followed by PC with 87.93%. PES showed an average transmittance of 70.43% and PEN with the lowest transmittance of 85.78%. As observed in Figure 5, upon deposition of CuNWs and AZO-NFs, there was a small shift of the spectra towards lower wavelengths. This shift is an indication of the increase in optical band gap of the materials. Furthermore, this observation suggests that the PET substrate would be able to transmit more light and thus be more efficient in the harvesting of light which is ideal for solar cell applications.

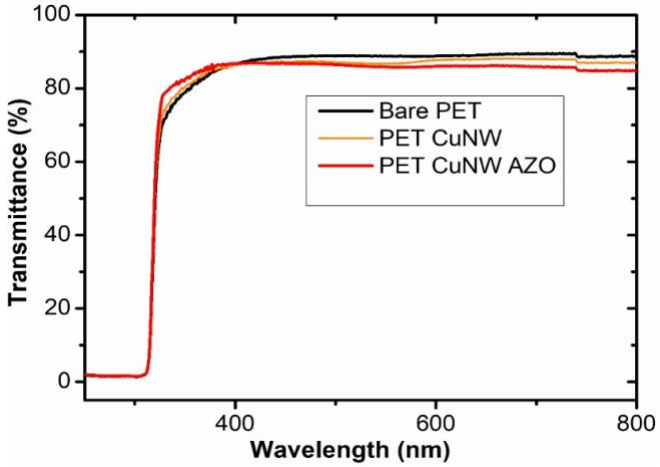

Figure 5: Transmittance spectra of PET substrate, PET coated with CuNWs and PET/CuNWs coated with AZO-NFs.

3.5 Mechanical (stress-strain) properties

Mechanical properties of bare polymer substrates, CuNWs and CuNWs/AZO-NFs were examined and are shown in Figure 6(a-d). Flexible and soft electronic devices are more favourable as the cell gets thinner, resulting in them becoming more prone to getting damaged. A flexible substrate will allow the device to take more strain and damage

DOI: https://doi.org/10.26799/cp-sms-nanomed-sensors-2023

compared to a rigid substrate which will not withstand the applied energy as readily. In order to get a better understanding, some of the parameters are illustrated in Figure 6(a). For the substrates flexibility and tensile strength tests for PC (1 mm), PES (0.25 mm), PEN (0.125 mm) and PET (0.1 mm) polymer substrates which have been coated with CuNWs and AZO-NFs as potential bottom electrodes are examined. The stress-strain graph in Figure 6(a) enables some of the parameters such as the yield strength, fracture strength and ultimate strength of the substrate to be determined.

The yield strength is an indication of how much energy a substrate can withstand before it becomes permanently deformed [15]. From Table 2 (PET and PEN substrates only shown), it can be seen that by the addition of the various layers the yield strength of the substrate is improved. For the CuNWs, this was linked to the interconnected nanowire network that covers the entire substrate and thus adding to its strength and improving the elasticity of the substrate. From these results PET is found to be one of the best overall yield strengths and PEN also having a strong yield strength After the yield strength the next major point the substrate can reach is the ultimate strength which is defined as the maximum stress a substrate can undergo before it either goes through necking or simply breaks. Beyond the ultimate stress the substrate is no longer viable and will not be able to support or protect the device further [15]. For the purpose of this study the ultimate strength will be viewed as a safety net for the potential soft electronic device, preventing it from breaking in such a manner that the other layered components of it would leak out should it become damaged. This is especially important as certain layers of solar cell devices contain toxic components (such as the lead in perovskite) that if it comes into contact with water and leaks out, could do damage to both the environment and to any person that come into contact with it. PET and PEN polymer substrates have substantially higher ultimate strength values. Once more, it can be observed that the addition of the CuNWs generally improves the ultimate strength value with its interlacing network which was observed in the SEM measurements.

The Young's Modulus is an important parameter to know for materials as it is an indication of its strength and how the material will behave in potentially different loads. The addition of the CuNWs and the AZO-NFs generally increases the value which indicates an increase of the overall strength of the film which further supports the previous analysis with the yield and ultimate strength. Furthermore, the Young's Modulus is also an indication of how ductile a material will be with a lower value behaving more ductile while a larger one is more brittle [15]. The modulus of resilience is also observed. The resilience of a material is the total energy a material can absorb and still return to its original shape without any deformations [16]. The greater this value is the more resilient the material is and thus the more energy it can safely absorb and be able to return to its original shape and form. This is important for application in small flexible devices as while the deformation of the film has limited impact on the structure and stability of the film. the addition of the CuNWs and the AZO-NFs result in an improvement of the resilience further indicating that the addition of these layers strengthens the properties of the substrate.

DOI: https://doi.org/10.26799/cp-sms-nanomed-sensors-2023

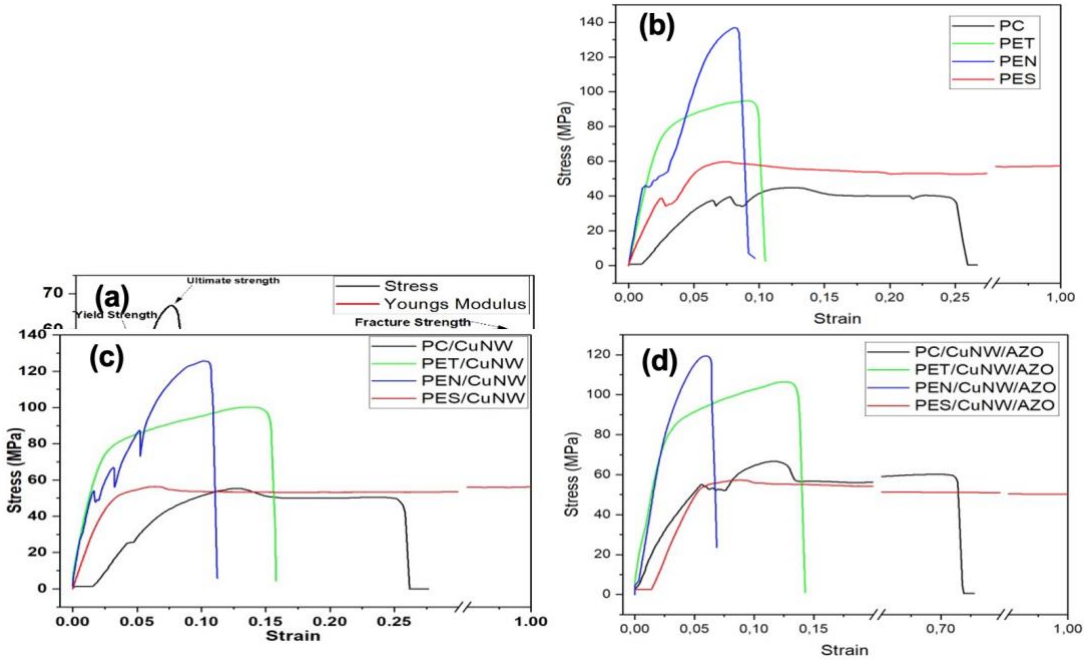

Figure 6: Mechanical (stress-strain) properties (a) Illustration of the general stress-strain plot and (b) from the polymer substrates, (c) from the polymer substrates with CuNWs and (d) from the polymer substrate/CuNWs/AZO.

Table 2: stress- strain parameters from PET and PES prepared electrodes.

PET				
	Yield Strength (MPa)	**Ultimate Strength (MPa)**	**Young's modulus (MPa)**	**Resilience (J/mm3)**
Bare substrate	68.866	94.772	3392.414	0.849
Substrate/CuNWs	71.715	100.258	3335.548	1.050
Substrate/CuNWs/AZO	75.253	106.460	3586.366	1.059
PEN				
	Yield Strength (MPa)	**Ultimate Strength (MPa)**	**Young's modulus (MPa)**	**Resilience (J/mm3)**
Bare substrate	46.182	136.887	4170.637	0.365
Substrate/CuNWs	54.032	146.764	4147.937	0.556
Substrate/CuNWs/AZO	78.814	119.411	4148.278	0.762

4. Conclusion

Smooth and ultra-long CuNWs were successfully synthesized and deposited on various polymer substrates. Their structure, morphology, optical and mechanical properties were investigated for possible application in soft electronic devices. The CuNWs were also coated with a layer of AZO-NFs to serve as a protective layer against possible oxidation. The XRD results confirmed the (111) cubic structure of the CuNWs. UV-VIS results indicated that the PET

DOI: https://doi.org/10.26799/cp-sms-nanomed-sensors-2023

polymer substrates have excellent light transmittance even when coated with a thin layer of CuNWs and AZO-NFs. AFM results showed that the additional layering of the nanoflakes increases the roughness of the films which could be beneficial for light trapping in applications such as flexible organic solar cells. The mechanical (stress-strain) properties of the polymer substrates were also investigated, bare and also with the deposition of CuNWs and AZO-NFs layers onto the substrates. From this data it can be observed that a PET and PEN based substrate would be the optimal choice for a flexible transparent substrate/electrode as they showed better results for the yield strength, Young's Modulus and resilience.

Acknowledgements

The authors would like to thank the University of South Africa (UNISA) for financial support and providing research infrastructure to conduct this research.

References

1. Wang X, Zhi L, Müllen K, "Transparent, Conductive Graphene Electrodes for Dye-Sensitized Solar Cells", *Nano Lett*, vol 8, pp.323–327, 2008.
2. Wang J, Liang M, Fang Y, Qiu T, Zhang J, Zhi L, "Rod-Coating: Towards Large-Area Fabrication of Uniform Reduced Graphene Oxide Films for Flexible Touch Screens", *Advanced Materials*, vol 24, pp.2874–2878, 2012.
3. Xu W, Gong Y, Liu L, Qin H, Shi Y, "Can graphene make better HgCdTe infrared detectors?", *Nanoscale Res Lett*, vol 6, pp. 1–4, 2011.
4. Wu J, Agrawal M, Becerril HA, Bao Z, Liu Z, Chen Y, Peumans P, "Organic Light-Emitting Diodes on Solution-Processed Graphene Transparent Electrodes". *ACS Nano*, vol 4, pp.43–48, 2010.
5. DeMeo D, MacNaughton S, Sonkusale S, Vandervelde T, "Electrodeposited Copper Oxide and Zinc Oxide Core-Shell Nanowire Photovoltaic Cells". In: Hashim A (ed) Nanowires - Implementations and Applications. InTech, pp.141–156, 2011.
6. Siebentritt S, "Wide gap chalcopyrites: material properties and solar cells", *Thin Solid Films*, vol 403–404, pp. 1–8. 2002.
7. Erlat AG, Yan M, Duggal AR, "Substrates and Thin-Film Barrier Technology for Flexible Electronics". In: Wong W, Salleo A (eds) Flexible Electronics: Materials and Applications. Springer Science & Business Media, pp 413–449, 2009.
8. Carlson DE (1989) Amorphous-silicon solar cells. IEEE Trans Electron Devices 36:2775–2780
9. Shang K, Gao J, Yin X, Ding Y, Wen Z , "An Overview of Flexible Electrode Materials/Substrates for Flexible Electrochemical Energy Storage/Conversion Devices." *Eur J Inorg Chem*., pp. 606–619, 2021.
10. C. Mayousse, C. Celle, A. Carella, J.-P. Simonato, "Synthesis and purification of long copper nanowires. Application to high performance flexible transparent electrodes with and without PEDOT:PSS", *Nano Res.*, vol 7, pp. 1–10, 2014.`
11. Y. Wang, P. Liu, B. Zeng, L. Liu, J. Yang, "Facile Synthesis of Ultralong and Thin Copper Nanowires and Its Application to High-Performance Flexible Transparent Conductive Electrodes", *Nanoscale Res Lett*., vol 13, pp. 1–10, 2018.
12. C. Kang, S. Yang, M. Tan, C. Wei, Q. Liu, J. Fang, G. Liu, "Purification of Copper Nanowires To Prepare Flexible Transparent Conductive Films with High Performance", *ACS Appl Nano Mater*., vol1, pp. 3155–3163, 2018.
13. J. Jiu, T. Araki, J. Wang, M. Nogi, T. Sugahara, S. Nagao, H. Koga, K. Suganuma, E. Nakazawa, M. Hara, H. Uchida, K. Shinozaki, "Facile synthesis of very-long silver nanowires for transparent electrodes", *J. Mater. Chem. A.*, vol 2, pp .6326–6330, 2014.
14. C. Preston, Y. Xu, X. Han, J.N. Munday, L. Hu, "Optical haze of transparent and conductive silver nanowire films", *Nano Res*., vol 6, pp. 461–468, 2013.
15. K. Balani, V. Verma, A. Agarwal, R. Narayan, Physical, Thermal, and Mechanical Properties of Polymers, in: Biosurfaces: A Materials Science and Engineering Perspective, Wiley: Hoboken, New Jersey, 2015: pp. 329–344.
16. C.-Y. Lin, J.-H. Kang, Mechanical Properties of Compact Bone Defined by the Stress-Strain Curve Measured Using Uniaxial Tensile Test: A Concise Review and Practical Guide, *Materials*., vol 14, pp.1–16, 2021.

Proceedings of the SMS/NanoMed/Sensors 2023 International Joint Conference
Albufeira, Portugal – October 25 – 27, 2023
DOI: https://doi.org/10.26799/cp-sms-nanomed-sensors-2023

Tactile Perception of Virtual Surfaces generated by Piezoelectric Actuators

Cyril Bertheaux[1], Ioan Alexandru Ivan[1,2], Daniel Ruiz-Lopez[3], Lucas Quiblier[2],
Jean-Christophe Roux[1], Roland Fortunier[1]

[1]Univ Lyon, Centrale Lyon, CNRS, ENTPE, LTDS, UMR5513, ENISE,
58 rue Jean Parot, 42023 Saint-Etienne, France, roland.fortunier@enise.ec-lyon.fr
[2]Institut National de Physique des Matériaux
405A Atomistilor, PO box MG-7, 077125 Magurele, Ilfov, Romania
[3]National Technological Institut, dept of biochemical engineering
Antonio García Cubas 600, Fovissste, 38010 Celaya, Gto., Mexico

Abstract

Virtual surfaces generated by the vibration of piezoelectric actuators were proposed for tactile exploration to a panel of persons. A set of vibration intensities was used to generate amplitudes from 2.5µm to 20µm, while frequencies were chosen between 5Hz and 45Hz. Each participant was asked whether he felt or not the generated signal, and the limit of his tactile perception was plotted on a frequency-amplitude diagram. A statistical analysis of these diagrams shows classically that the mean frequency of tactile perception decreases when the amplitude is increased. However, when intensity variations are generated at given frequencies, the tactile perception presents a local maximum at 10Hz, then decreases, and finally increases again after 20Hz. This result agrees with the frequencies of the Merkel and Meisner mechanoreceptors i.e., less than 10Hz and above respectively. The use of piezoelectric actuators as virtual surfaces seems to be a promising and easy way to quantify tactile perception. This system is also developed to simulate dynamic touch, by using out-of-phase vibrations and a better spatial resolution.

Keywords: Haptic, Virtual, Perception, Actuators, Piezoelectric

1. Introduction

The haptic system can be described as a set of coordinated processes of perception and action associated with the sensation of touch and kinaesthesia. It allows to generate controlled movements of the limbs and other parts of the body [1]. Kinaesthetic feedback is associated with the interaction of muscles, joints, and tendons, to provide feedback about weight, stretch, body position…, while tactile feedback allows the perception of stimuli on the skin such as vibration, pressure, texture… [2].

A fundamental part of haptic perception is texture recognition, as humans can distinguish different surface properties of an object through the sensory characteristics of the skin. Texture perception results from the ability of humans to process and interpret exteroceptive sensations, generated by the characteristics of the objects with which they interact during tactile exploration [3]. The human sense of touch is thus a very complete sense, allowing us to experience many sensations, either pleasant or unpleasant [4], such as physical and mechanical properties of objects, temperature...

Information that incorporates the perception of a texture can be generated by two different mechanisms of tactile exploration. When the finger comes into contact with the object to be characterized, we speak of direct touch, whereas if the information of the texture is presented through a probe that interacts with the object, we speak of indirect touch [5]. Moreover, tactile exploration can be static or dynamic, depending on whether there is a tribological movement between the fingertip and the surface or only a quasi-static contact [6].

It has been determined that, during the process of tactile exploration, the finger perceives vibrations and deformations caused by the friction between the skin and the physical characteristics of the surface [7]. These vibratory stimuli must respect a given frequency and intensity to activate the sensory receptors and generate the spatial information of the material touched [8,9,10].
Consequently, it has been decided to explore the possibility to generate stimuli by the vibration of piezoelectric actuators, to simulate the tactile exploration of virtual surfaces. In this paper, we present the first results obtained with these actuators: the static and direct tactile exploration of virtual surfaces, with a particular emphasis on the limit of tactile detection. The characteristics of the system are first presented. Then this system is applied to the detection of tactile perception. The results are presented and discussed.

DOI: https://doi.org/10.26799/cp-sms-nanomed-sensors-2023

1. Materials and Method

A first experiment has been carried out with a vibrating touch screen to quantify the limit of tactile perception [11]. The results give for different amplitudes and shapes of the signal the minimum frequency felt by the panellist. It is found that this minimum frequency decreases from 40Hz to 5Hz when the amplitude is increased from 4µm to 79µm. However, the frequency ranges associated with the human mechanoreceptors have not been explored.

Mechanoreceptors are discs (Merkel) and corpuscles (Meissner, Ruffini and Pacini), which perform transduction and transmission of tactile feedback to the brain. Those with slow adaptation are triggered throughout the stimulus (Merkel, Ruffini), while those with rapid adaptation are triggered at the beginning and at the end of a stimulus (Meissner, Pacini). Some of them (Merkel and Meissner, referred to as type I) have small receptive fields, clear borders as ending, and are mainly located in the area of the finger pulp, whereas the others (Ruffini and Pacini, referred to as type II) present larger receptive fields and less clear borders. Accordingly, type I mechanoreceptors are excited at relatively low frequencies, typically below 10Hz for the Merkel discs, and from 10Hz to 50Hz for the Meissner corpuscles, while types II react at larger frequencies, namely 30Hz to 400Hz for the Ruffini corpuscles, and 100Hz to 500Hz for the Pacini corpuscles [12, 13].

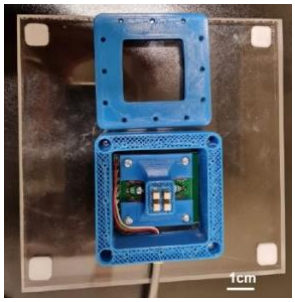

Figure 1: Experimental set-up

The experiment presented in this paper is aimed at detecting the minimum amplitude for which a fixed frequency vibration signal is felt via the type I mechanoreceptors (Merkel discs and Meissner corpuscles). As a consequence, frequencies are varied from 5Hz to 45Hz with 5Hz steps, and, for each frequency, the signal amplitude is reduced until the panellist declares that he no longer feels the signal.

The experiments were performed with a haptic device made of four piezoelectric actuators (Piezoelectric Stack 150V~33 µm) arranged in a 2D printed box, which itself is screwed onto a support to stabilize it and avoid parasitic vibrations (Figure 1). The actuators oscillate vertically in phase. The vibration is generated by a sinusoidal tension signal sent at a given frequency, thanks to a MatLab code coupled with an amplificatory (x30). During the experiments, a latex glove is positioned on these actuators to ensure the safety of the panellists.

The vibration amplitudes were calibrated as a function of the applied tension. The results are given in table 1. The amplitudes used vary from 20.0µm to 2.5µm. These relatively small values are due to the limited possibilities offered by the actuators, when the tension remains below 100V.

Amplitude (µm)	2.5	4.1	6.0	8.8	10.8	13.1	15.3	17.8	20.0
Voltage (V)	15	23	32	42	51	61	72	84	96

Table 1: Calibration of the amplitude of the vibrating signal

During the test, the participant was asked to position himself comfortably, with a minimal tension in his arm, while applying a weak force to the device by the finger of its dominant hand. The experiment is then explained to him. For each frequency, the participant must indicate when he no longer feels a vibration signal. Thus, for each participant, a frequency-amplitude matrix is filled with zeros when the signal is not felt and ones when it is felt. A panel of 69 participants was used for this experiment. It was made of 44 men and 25 women aged from 16 to 61.

The perception threshold is defined as the minimum intensity for which a stimulus will generate a change in the observer's perception [13]. There are several thresholds, corresponding to perceived intensities of the

DOI: https://doi.org/10.26799/cp-sms-nanomed-sensors-2023

stimulus, and resulting on different interpretations of it (figure 2). If the stimulus intensity is too low, it merges with the ambient noise in the infraliminar zone. When the threshold of subliminal perception is exceeded, the stimulus can be perceived randomly in the liminar zone. The sensation becomes clear only when the stimulus exceeds the threshold of absolute perception to enter in the supraliminal zone. Finally, the sensation is perceived with a constant and strong intensity in the saturation zone [11]. According to this progressive perception, the statistical analysis of our experimental data are expected to present a relatively large standard deviation.

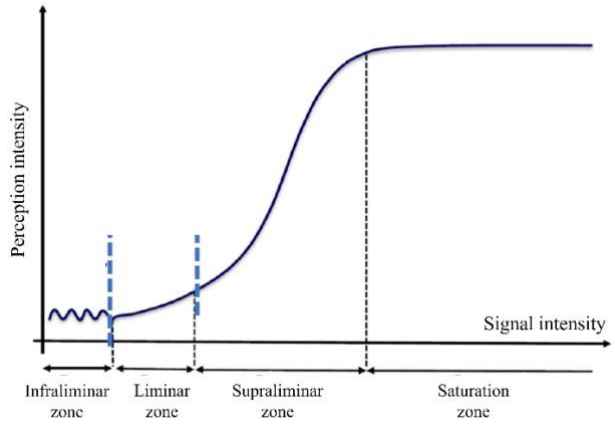

Figure 2: Perception threshold

2. Results and Discussion

Figure 3 gives typical results obtained with one participant. It can be observed that, at low frequencies, the signal is never felt. In the case depicted in figure 3, the perception threshold of the participant cannot be determined below 20Hz.

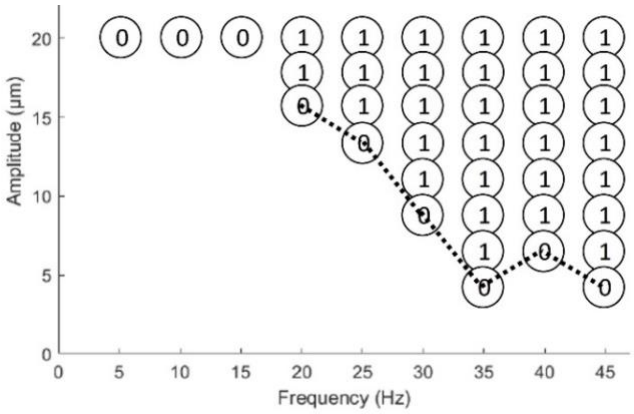

Figure 3: Typical tactile perception curve obtained for one participant.

However, the frequency-amplitude matrices (figure 3) of the 69 participants can be added to obtain the global answering surface of the panellists. Figure 4 gives the percentage of panellists feeling the signal at given frequencies and amplitudes. The vibration is always felt (100%) for high frequencies and large amplitudes, and the percentage decreases at lower frequencies, or when the amplitude is decreased. It can be observed in this figure that the answering surface associated with women (figure 4b) exhibits a local maximum for large amplitudes, when frequencies are around 10Hz. This 10Hz frequency is commonly used as the reference frequency for the Merkel tactile mechanoreceptor, while the Meissner mechanoreceptors act above.

DOI: https://doi.org/10.26799/cp-sms-nanomed-sensors-2023

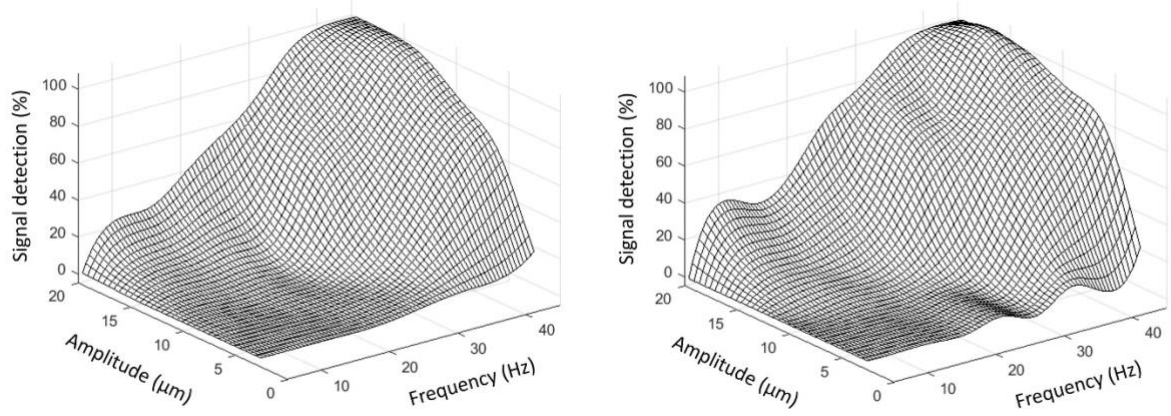

4a. Men and Women 4b. Women

Figure 4: Answering surfaces of the experiment.

A first statistical analysis was performed by using the histograms depicted in figures 5. The frequency is fixed, and, for each amplitude, the histogram gives the fraction of panellists feeling the signal until this amplitude, but not for smaller values. The histogram is then fitted by a lognormal distribution function (solid line in figure 5). It can be seen that, at low frequency (e.g. 20Hz in figure 5), the distribution function gives results that should have been obtained at large amplitudes. This allows to define a median value of the distribution above the amplitudes used for the experiment, for example 22.22 µm at 20Hz in figure 5.

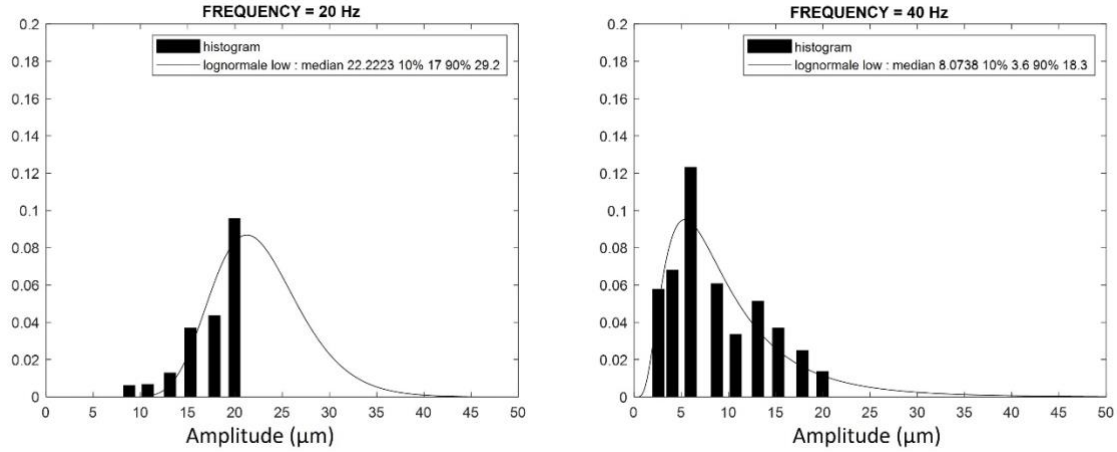

Figure 5: Histogram and fitted lognormal distribution function for two excitation frequencies.

This statistical analysis is performed according to the experimental procedure, in which the amplitude is varied at different frequencies. However, the local maximum depicted in figure 4b cannot be exhibited by this method. As a consequence, a second statistical analysis was performed, in which the frequency is varied at different fixed amplitudes.

The results of the second statistical analysis are depicted in figure 6. In order to take into account, the local maximum depicted in figure 4b, the histograms were fitted with a distribution function made of two weighted gaussian curves. At low amplitudes (e.g. 4µm in figure 6), this local maximum does not appear, and the distribution function is made of a unique gaussian curve. At large amplitudes (e.g. 17.8µm in figure 6), two weighted gaussian curves are necessary to fit the histogram, and the local maximum can be associated with the dashed line, at 10Hz frequency.

DOI: https://doi.org/10.26799/cp-sms-nanomed-sensors-2023

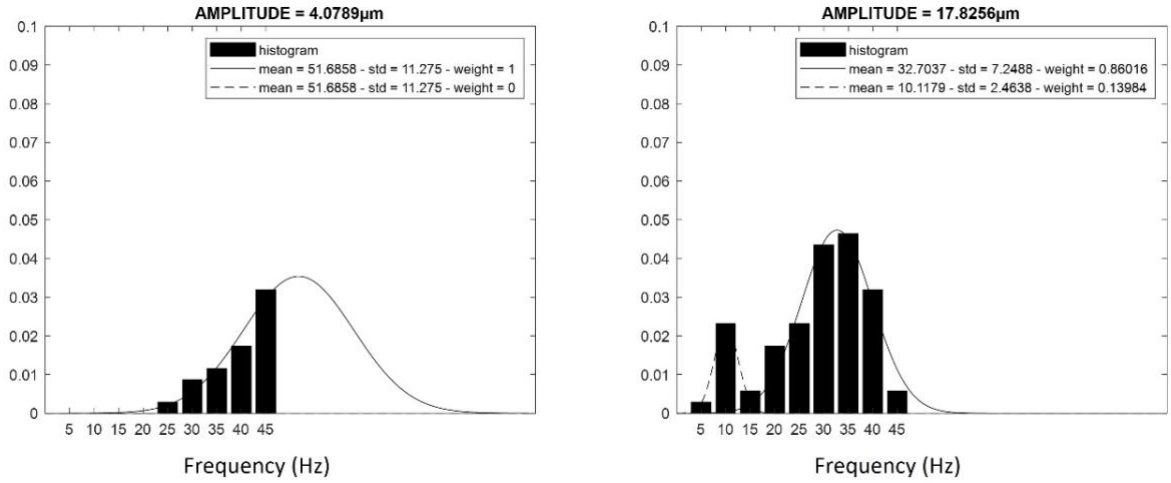

Figure 6: Histogram and fitted distribution function for two excitation amplitudes.

This second statistical analysis allows for drawing perception domains associated with the Meissner and the Merkel mechanoreceptors. These domains are drawn in figure 7, together with the results obtained in a previous study [11]. In this figure, the mean values (solid lines) and the 10% - 90% confidence values (dashed lines) are given. It can be seen that the results obtained in this study are globally in agreement with the previous study [11], and that more detailed perception domains can be identified when the mechanoreceptors are considered.

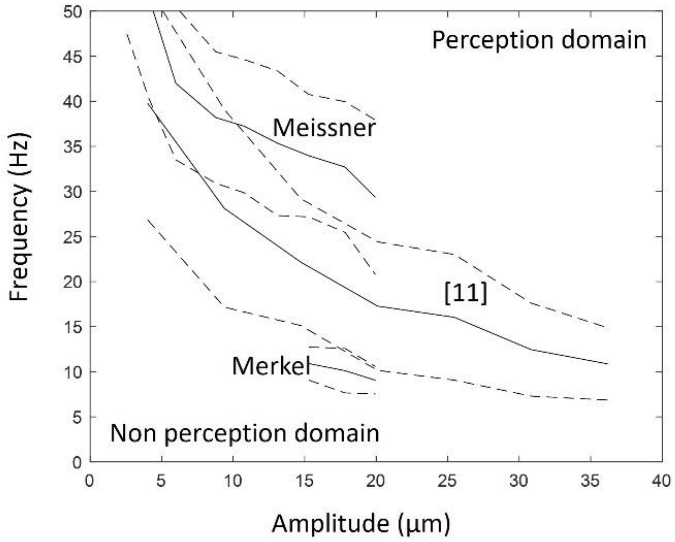

Figure 7: Perception domain in a Amplitude-Frequency diagram

3. Conclusion

The tactile perception domain was determined by analysing the results obtained with 69 panellists giving their feeling of a vibrating signal produced by piezoelectric actuators. The obtained answering surface exhibits a local maximum that has been analysed by using a distribution function made of two weighted gaussian curves. The results are in global agreement with a previous study [11], but the perception domains seems to be dependent on the mechanoreceptor considered.

The use of piezoelectric actuators to simulate actual surfaces seems to be a promising way, leading to the development of a prototype for virtual touch. However, to achieve this prototype, a better spatial resolution and larger signal amplitudes have to be obtained. This work is in progress, together with the manufacturing of model surfaces associated with these signals.

DOI: https://doi.org/10.26799/cp-sms-nanomed-sensors-2023

References

1. S. Biswas and Y. Visell, “Haptic Perception, Mechanics, and Material Technologies”, *Advanced Functional Materials,* vol. 31, no. 39, pp. 2008186, 2021
2. Y. Huang, K. Yao, J. Li, D. Li, H. Jia, Y. Liu and X. Yu, X, “Recent advances in multi-mode haptic feedback technologies towards wearable interfaces”, *Materials Today Physics,* vol. 22, 100602, 2022
3. E. Altinsoy and S. Merchel, “Electrotactile feedback for handheld devices with touch screen and simulation of roughness”, *IEEE Transactions on Haptics*, vol. 5, no. 1, pp 6-13, 2011
4. M. A. Heller and E. Gentaz, “Psychology of Touch and Blindness”, *Psychology Press*, New-York, 2013
5. M. Hollins, F. Lorenz and D. Harper, “Somatosensory coding of roughness: the effect of texture adaptation in direct and indirect touch”, *Journal of Neuroscience*, vol. 26, no. 20, pp 5582-5588, 2006
6. L.A. Jones and H.Z. Tan, “Application of psychophysical techniques to haptic research”, *IEEE transactions on haptics,* vol. 6, no. 3, pp 268-284, 2013
7. K. Ito, S. Okamoto, Y. Yamada and H. Kajimoto, “Tactile texture display with vibrotactile and electrostatic friction stimuli mixed at appropriate ratio presents better roughness textures”, *ACM Transactions on Applied Perception (TAP),* vol 16 no. 4, pp 1-15, 2019
8. S. Bensmaia and M. Hollins, “Pacinian representations of fine surface texture”, *Perception & psychophysics*, vol. 67, no. 5, pp 842-854, 2005
9. P. Strohmeier and K. Hornbæk, “Generating Haptic Textures with a Vibrotactile Actuator”, *Proceedings of the 2017 CHI* Conference on Human Factors in Computing Systems, 4994-5005, 2017
10. X. Yan, Q. Wu, G. Liu and X. Sun,“Improving the tactile perception of image textures based on adjustable amplitude, frequency, and waveform”, *The Visual Computer*, vol. 37, no. 6, pp 1297-1308, 2020
11. C. Chauvelin, Th. Sagi, Ph. Coni, J.M. André, Ch. Jauze and V. Lespinet-Najib, “Haptics on a Touch Screen: Characterization of Perceptual Thresholds”, *Int. J. of Human-Computer Interaction*, vol. 30, no. 11, pp 872-881, 2014
12. R.S. Johansson and A.B. Vallbo, “Tactile sensory coding in the glabrous skin of the human hand” *Trends in neurosciences*, vol. 6, pp 27-32, 1983
13. R.K. Ray and M. Manivannan, "Spatial summation of electro-tactile displays at subthreshold." *Proc. 4th Int. Conf. on Human Interaction and Emerging Technologies*, Strasbourg, Springer International Publishing, 2021